Revision 2

Crystallization of groundmass nanolites in the 2011 Shinmoedake eruption

Mayumi Mujin[1,*], Michihiko Nakamura[1], and Akira Miyake[2]

[1]Department of Earth Science, Graduate School of Science, Tohoku University, 6-3, Aramaki-Aza-Aoba, Aobaku, Sendai 980-8578, Japan

[2]Department of Geology and Mineralogy, Graduate School of Science, Kyoto University, Kitashirakawaoiwake-cho, Sakyo-ku, Kyoto 606-8502, Japan

ABSTRACT

Crystallization of groundmass minerals may record the physicochemical conditions of magmatic processes upon eruption and is thus a topic of interdisciplinary research in the disciplines of mineralogy, petrology, and volcanology. Recent studies have reported that the groundmass crystals of some volcanic rocks exhibit a break in their crystal size distribution (CSD) slopes that range from a few micrometers to hundreds of nanometers. The crystals consisting of the finer parts of the break were defined as nanolites. In this study, we report the presence of nanometer-scale crystals down to 1 nm in the pyroclasts of the 2011 eruption of Shinmoedake, the Kirishima volcano group, based on field emission-scanning electron microscopy (FE-SEM) and transmission electron microscopy (TEM).

We discovered a gap (hiatus) from ~100 to ~30 nm in the size distribution of pyroxene in a dense juvenile fragment of a Vulcanian explosion. The pyroxene crystals ~20–30 nm on a diameter were ferroaugite ($C2/c$), while those a few hundred nanometers in width had a composite structure consisting of the domains of orthopyroxene (*Pbca*), augite ($C2/c$), and sub-calcic augite ($C2/c$). In high-angle annular dark-field scanning TEM images of the same sample, bright spots ~1–2 nm in diameter were recognized with a gap in size from ~10–20 nm titanomagnetite ($Fd\bar{3}m$). They are presumed to have Fe-rich compositions, although their phases were too small to be determined. In addition, we found that crystals smaller than a few tens of nanometers for pyroxene and one hundred nanometers for plagioclase did not exist or their number densities were too low for accurate determination. This indicates that there are practical minimum sizes of the crystals. These observations show that nucleation of the nanoscale crystals almost paused (froze) in the late stage of groundmass crystallization, possibly due to a decrease in undercooling, increase in interfacial free energy, and decrease in diffusivity in a dehydrated melt, whereas crystal growth was mostly continuous. In this paper, we introduce the novel term "ultrananolite", to refer to crystals smaller than 30 nm in diameter, and redefine "nanolite" simply as those 30 nm–1 μm in width, complementing the size interval of crystals in volcanic groundmass smaller than

microlites (1–30 μm). In the transient nucleation process, the presence of subcritical size clusters is required. The observed ultrananolite-sized particles might partly include subcritical clusters. The difference in the slope of CSDs, presence of gaps in size distribution and minimum crystal size among the eruption styles of the 2011 Shinmoedake eruption may be interpreted by considering the difference in magma residence time and fragmentation pressure in the shallow conduit, and possibly the rewelding process in the crater.

Keywords: Microlite, Nanolite, Ultrananolite, Crystal size distribution, transient nucleation, Vulcanian explosion

INTRODUCTION

Although nanoscale crystals present in the groundmass of volcanic rocks have long been recognized as “cryptocrystals” (e.g., Johannsen, 1931), their mineralogical characteristics have been poorly described. Limited petrological studies on nanoscale crystals include those on the origin of the brownish color (Schlinger et al., 1986; Paulick and Franz, 1997) and remnant magnetism (Schlinger et al., 1988) of volcanic glasses that contain nanoscale crystals of Fe-oxide. Sharp et al. (1996) obtained the crystal size distribution (CSD) of pyroxene in the groundmass of the Ben Lomond rhyolite lava dome down to a scale of 100 nm and found a pronounced break of the

55 CSD at 600 nm in width. They termed the smaller group of crystals "nanolites" and
56 reported a core–rim structure showing pigeonite and augite overgrowths on
57 hypersthene.

58 Because nanolites crystallize at low pressure, they can elucidate near-surface
59 eruption dynamics. Mujin and Nakamura (2014) first reported the presence of
60 groundmass nanolites in quenched pyroclasts from the 2011 eruption of Shinmoedake,
61 the Kirishima volcano group. They proposed that the nanolites recorded the
62 physicochemical conditions of magma at the point of the transition in eruption style.
63 However, nanolites in the 2011 Shinmoedake eruption products have not been fully
64 characterized in terms of crystallographic phases and solid solution composition; such
65 parameters are essential for further clarifying their crystallization conditions. In this
66 study, we investigated in detail the 2011 Shinmoedake eruption products examined by
67 Mujin and Nakamura (2014). We discovered finer sized crystals of pyroxene (~20–30
68 nm) and most likely Fe–Ti oxide or amorphous cluster (~1–2 nm) with a clear size gap
69 (hiatus) in a dense juvenile fragment of the Vulcanian explosion. We introduce the term
70 "ultrananolite" to refer to crystals smaller than 30 nm in diameter. We redefine
71 "nanolite" alternatively as crystals 30 nm–1 μm in width. We obtained the chemical
72 compositions and crystal space groups of pyroxene nanolites ~1 μm in width and those

of pyroxene and Fe–Ti oxide ~20–30 nm and ~10–20 nm on a diameter, respectively. The areal number density measurements of pyroxene and Fe–Ti oxide were extended to 1 nm. We then discuss the crystallization processes of nanolite and ultrananolite in terms of nucleation mechanism and phase diagrams. Finally, their implications for the shallow magma ascent processes of the 2011 Shinmoedake eruption are discussed.

OUTLINE OF THE 2011 SHINMOEDAKE ERUPTION

The Shinmoedake volcano is part of the Kirishima volcano group located in southern Kyushu, Japan (Figs. 1a and 1b). The main phase of eruption activity in 2011 is characterized by sub-Plinian eruptions and subsequent lava extrusion with intermittent Vulcanian explosions from January 26 to 31 followed by frequent Vulcanian explosions from February 1 to March 13 (Miyabuchi et al., 2013; Kozono et al., 2013). This eruption sequence is well documented by various geophysical observations. In the Appendix, we present a brief review of geophysical constraints on the magma ascent processes in the 2011 eruption of the Shinmoedake. In the evening of January 26 and the morning and evening of January 27, three major sub-Plinian eruptions were detected by weather radar eruption cloud echo measurements (Shimbori et al., 2013). Geodetic and synthetic aperture radar satellite (SAR) observation revealed that the sub-Plinian eruptions continued for 2.5 h, 2.5 h, and 1.75 h, respectively

(Kozono et al., 2013). From January 29 to 31, continuous growth of a pancake-shaped mass of lava inside the summit crater was detected by SAR imaging analysis (Ozawa and Kozono, 2013). In addition, 13 infrasound-generating Vulcanian explosions were reported from 15:41 JST (Japan Standard Time, UTC + 09:00) on January 27 to 19:23 on March 1 (Japan Meteorological Agency, 2012).

SAMPLE COLLECTION AND BASIC PETROGRAPHY

In this study, two dense juvenile fragments were examined by scanning electron microscopy (SEM) in addition to the samples examined by Mujin and Nakamura (2014); these rocks include six sub-Plinian pumice clasts, five Vulcanian pumice clasts, and three dense juvenile fragments. These samples were collected on July 24, 2011, at Takachihogawara, 3.0 km south of the Shinmoedake crater. Brown, gray, and white colored pumice clasts were collected from a section of well-preserved sub-Plinian fall deposit. The sub-Plinian pumices used in this study were collected from a well-sorted pumice fall deposit (layers 2–5 of Nakada et al., 2013). The fine ash of the January 27, 15 h 41 min Vulcanian explosion (unit 3L of Miyabuchi et al., 2013) was excluded. The Vulcanian products were collected from the topmost surface of the pumice deposits of the three sub-Plinian eruption columns (layer 5 of Nakada et al., 2013; unit 3U of Miyabuchi et al., 2013), which consist of glassy, dense juvenile

(co-magmatic) fragments of lava and gray–brown pumices that are clearly coarser than the pumices of the sub-Plinian eruption deposit. The well-preserved nature of the original deposition was confirmed by their jigsaw impact cracks (Fig. 1c). The explosion date of the Vulcanian sample has not been determined; however, the wind direction and the eruption cloud height reported in the Volcanic Activity Documents by the Japan Meteorological Agency (JMA, 2011) indicate likely dates of February 1, February 11, and March 13, 2011. We also collected a chip of glossy volcanic breccia (projectiles) tens of centimeters on a side that formed impact craters on the surfaces of fallout pumice deposits at Nakadake summit, 1.1 km south of the Shinmoedake crater, on July 23, 2015. Suzuki et al. (2013) reported that the gray and brown pumices and dense juvenile fragments are similar in bulk chemical composition (SiO_2 = 57–58 wt%), whereas the white pumice (SiO_2 = 62–63 wt%) is a dacitic endmember of the mixed magma that formed the majority of the 2011 andesite.

The interstitial glass in the groundmass was almost colorless in the sub-Plinian and Vulcanian pumices and light brown–brown in a dense fragment. However, the bulk groundmass compositions including groundmass minerals were almost the same for the pumices from the sub-Plinian eruption and pumices and dense juvenile fragments of the Vulcanian explosions, at SiO_2 = 63–64 wt% (Mujin and Nakamura, 2014). The

127 petrographic features of the volcanic breccias from the Nakadake summit were similar
128 to those of the dense juvenile fragments collected at the Takachihogawara. Low
129 (×5,000) and high (×10,000–40,000) magnification backscattered electron (BSE)
130 images of the three types of samples are shown in Figure 2. The principle petrographic
131 features of these samples were reported by Mujin and Nakamura (2014). The modal
132 compositions of plagioclase microlite and nanolite in the groundmass of the three
133 erupted materials are similar at 20–26 area%. The modal compositions of pyroxene
134 microlite and nanolite are 9–13 area%. Using these values and bulk-rock manometric
135 analyses of water content, the water contents in the interstitial glasses of the sub-Plinian
136 pumices, Vulcanian pumices, and dense fragments were recalculated to be 0.35, 0.47,
137 and 0.44 wt%, respectively (Mujin and Nakamura, 2014).

138 **ANALYTICAL PROCEDURES**

139 **FE-SEM-EDS analyses**

140 For SEM analysis, the cut surfaces of samples were polished using alumina
141 powder with a grain size of 0.3–1.0 μm. The flaws and damages caused by mechanical
142 polishing were removed by an Ar-ion milling apparatus (Model 691, GATAN PIPS),
143 with an acceleration voltage of 5 kV at an incident angle of 3° for 10 min, in order to
144 obtain clear SEM images at a magnification of > ×10,000. We obtained digital BSE

145 images of the polished sections at Tohoku University by using an SEM instrument with
146 tungsten filament (W-SEM; S-3400N, Hitachi High-Technologies) at an acceleration
147 voltage of 15 keV. In addition, we used in-lens type high-resolution field emission
148 (FE)-SEM instruments, Hitachi High-Technologies S-5500 and SU9000 at Tohoku
149 University and Hitachi High-Tech Tokyo Solution Lab, respectively, at acceleration
150 voltages of 2–15 keV. For the higher magnification observations with FE-SEM, we
151 applied lower acceleration voltages.

152 **TEM observation**

153 For TEM analyses of a dense juvenile fragment, an ultrathin section was
154 extracted from a slab using a focused ion beam (FIB) system (Quanta 200_3DS, FEI) at
155 Kyoto University and was observed under a transmission electron microscope (TEM;
156 JEOL JEM-2100F) equipped with CCD cameras (Gatan Orius 200D and 1000D) and an
157 energy dispersive X-ray spectrometry (EDS; JEOL Silicon Drift Detector) system at
158 Kyoto University. In the FIB system, a Ga^+ ion gun was used at an acceleration voltage
159 of 30 kV and a beam current of 0.1–30 nA; a beam current of 48 pA at 5 kV was used
160 for the final processing. We conducted TEM observations and EDS analyses at an
161 acceleration voltage of 200 kV. For quantitative X-ray analysis of thin specimens in
162 (scanning; S)TEM, the ζ-factor method (Watanabe and Williams, 2006) was applied.

Prior to the quantification, the ζ factors were determined for this particular instrument by using a NIST standard reference material 2063a glass thin-film (Reed, 1993) as described in Watanabe and Williams (2006). For accurate electron beam current measurements required for the ζ-factor method, one of the CCD cameras was used with appropriate calibration beforehand. The concentration of oxygen in atomic percent was quantified independently. The weight percent of the oxides was calculated from the atomic percent of cations and the molecular weight of oxides. The mineral phases were identified through space group determination with diffraction analyses and by quantitative analyses of chemical compositions. The raw EDS counts of pyroxene, ~20–30 nm on a diameter, were rich in silicon and oxygen compared with the stoichiometric composition owing to the effect of the surrounding glass. To obtain the solid solution compositions, we therefore subtracted the glass composition from the raw data to fit the pyroxene stoichiometry. We used the most differentiated glass composition obtained by spot analyses with W-SEM-EDS in the calculation. Because the concentrations of MgO, FeO, and CaO in the glass were low, the overlapping effect on the solid solution composition was not significant.

SEMI-LOG CSD PLOTS

The semi-log CSD plots of groundmass plagioclase and pyroxene, after

181 stereological corrections with CSDCorrections (Higgins, 2000), are shown in Figure 3.
182 The raw data are the same as those in Mujin and Nakamura (2014), and the difference in
183 the plotting procedure from that in Mujin and Nakamura (2014) is presented in the
184 Appendix. The used data are crystals from 0.1 to 5.2 μm in width before
185 CSDCorrections is applied. We traced the crystals in the images manually and counted
186 number of the crystals because the crystals have compositional zoning and small
187 contrast with surrounding glass. The method for discrimination between glass and
188 crystals is presented in Mujin and Nakamura (2014). In Figure 3, the 3D shape of
189 crystals was estimated from the 2D size measurements with CSDSlice (Morgan and
190 Jerram, 2006) in order to correct the effects of intersection probability and
191 cut-sectioning (Table 1). The estimated aspect ratios of the crystal shape converged to a
192 narrow range for the same mineral, although not perfectly (Table 1). We used the aspect
193 ratio and number of bin/decade obtained from the ×5000 images of sub-Plinian pumices,
194 i.e., 1:1:8 and 5, respectively, for pyroxene, and 1:5:10 and 5 for plagioclase. By using a
195 common parameter, we were able to load two separate data sets obtained in different
196 magnifications with W-SEM and FE-SEM to CSDCorrections and produce a single line.
197 The general characteristics of CSDs do not change significantly even if we use different
198 aspect ratios and bin/decade numbers that best fit each data set. The difference in the

199 maximum crystals width between plagioclase and pyroxene (Fig. 3) resulted from the
200 difference in their crystal shapes. Detailed correction conditions are described in the
201 Appendix.

202 All the CSD plots showed a concave upward curvature (Fig. 3). It is known
203 that high-level stereological corrections, including CSDCorrections, may result in
204 excess correction of the number of small crystals (Castro et al., 2003). It should be
205 noted, however, that only the CSD slope of plagioclase in sub-Plinian pumices did not
206 increase with a decrease in size, as pointed out by Mujin and Nakamura (2014) (also see
207 Fig. S2).

208 **RESULTS**

209 **Chemical composition and space group of pyroxenes**

210 The chemical compositions of the pyroxenes are presented in Figure 4 and
211 Table 2. Figures 5a and 5b–5e show a high-angle annular dark-field scanning
212 transmission electron microscopy (HAADF-STEM) image and X-ray intensity maps of
213 Al, Fe, Mg, and Ca, respectively, for a pyroxene with a width of ~1 μm in the dense
214 juvenile fragment. This crystal is composed of at least three domains. The bright-field
215 TEM (BF-TEM) image and one of the selected area diffraction (SAD) patterns of each
216 domain taken at a common tilt angle are shown in Figures 5f–5i. The chemical

compositions of each domain are presented in Table 2. Based on the chemical compositions and SAD patterns, the phases can be determined as orthopyroxene (*Pbca*; Fig. 5g), Ca-rich augite (*C*2/*c*; Fig. 5h); and sub-calcic augite (*C*2/*c*; Fig. 5i). Such a composite pyroxene is not rare in the sample, although statistical counting was not conducted. In Figures 5a–5d, weak concentric compositional zoning was also observed.

A BF-TEM image and SAD patterns of three pyroxene crystals with a diameter of ~20–30 nm in the dense juvenile fragment are shown in Figure 6. The crystals were too small for determining the phase from a diffraction pattern of one particle. Based on the assumption that these pyroxenes have the same structure, the diffraction patterns correspond to the *C*2/*c* clinopyroxene structure. The zone axes for each diffraction pattern are shown in Figures 6b, 6c, and 6d. The chemical compositions of the pyroxenes ~20–30 nm on a diameter are enriched in iron compared with those for crystals ~1 μm in width, as shown in Figure 4 and Table 2.

Phase identification of Fe–Ti oxide

Figures 7a and 7b show BF-TEM images of a dense juvenile fragment with relatively lower and higher magnifications, respectively. Figure 7c shows a SAD pattern of an Fe–Ti oxide grain ~500 nm in width labeled in Figure 7a, which shows a twin structure and corresponds to the $[1\bar{1}0]$ zone axis of the $Fd\bar{3}m$ structure. Figure 7d shows

a Fourier transform image of an Fe–Ti oxide crystal ~10 nm on a diameter labeled in Figure 7b, which can be explained by the $Fd\bar{3}m$ structure with zone axis $[0\bar{1}1]$. The proportion of ferric and ferrous iron of the larger ~500 nm crystal was calculated to fit the charge balance assuming that the divalent, trivalent, and tetravalent cations are Mg, Mn, and Fe^{2+}; Al and Fe^{3+}; and Si^{4+} and Ti^{4+}, respectively (Table 3). The X-ray intensity maps of Fe, Ti, Si, Mg, and Ca (Fig. 8) show that the smaller ~10–20 nm crystals contain Ti, although the quantitative value was not obtained owing to the resolution limitation. These crystallographic and chemical data show that the Fe–Ti oxide both ~500 nm and ~10–20 nm in width are titanomagnetite.

Figures 9a and 9b show a BSE and HAADF-STEM images of a dense juvenile fragment from a Vulcanian explosion, respectively. The bright crystals in Figure 9 are titanomagnetite, as determined above. The bright spots in the HAADF-STEM image ~1–2 nm in diameter (Fig. 9b) have most likely Fe–rich compositions judging from their higher brightness in the HAADF-STEM image than that of pyroxene ~20–30 nm on a diameter. Whether these spots are crystalline or amorphous was not identified owing to resolution limitation.

Size ranges and number densities of nanolites and ultrananolites

Redefinition of nanolite and definition of ultrananolite. As shown in Figures

253 2f and 9, pyroxene and titanomagnetite ~10–30 nm on a diameter and Fe–rich oxide
254 spots <2 nm in diameter are included in the dense juvenile fragment sample. These
255 minute crystals were also observed in parts of the groundmasses of volcanic bombs
256 collected at the Nakadake summit. These crystals have clear size gaps from the larger
257 ones indicating hiatus; pyroxene of ~30–100 nm and Fe–Ti oxide of ~2–10 nm are rare.
258 Therefore, two gaps exist for Fe–Ti oxide; the other gap is from a few hundred
259 nanometers to ~20 nm. In the pumices of sub-Plinian eruptions and Vulcanian
260 explosions, crystals smaller than 30 nm were not found in the interstices of microlites
261 and nanolites of pyroxene and plagioclase (Figs. 2b and 2d).

262 Mujin and Nakamura (2014) differentiated nanolites from microlites based on
263 the kinks and gaps in the CSD, similar to the first definition of nanolite by Sharp et al.
264 (1996). In this paper, as noted previously, we redefine the term “nanolite” simply as
265 crystals of size 30 nm–1 μm in width, and “ultrananolite” as those < 30 nm in diameter,
266 so that this classification is consistent with those by Cashman (1992) (microlite, 1–30
267 μm; microphonocryst, 30–100 μm), avoiding the following problems. (1) The crystal
268 sizes at kinks and gaps in CSDs may vary among different minerals, magma
269 compositions, and crystallization processes. This leads to a situation in which minerals
270 in the same size range could be classified into different categories, which is confusing.

(2) One may identify nanolites and ultrananolites in their samples without obtaining CSD.

In the FE-SEM (BSE) and TEM (HAADF-STEM) images of Figure 9, some titanomagnetite ultrananolites overlap with pyroxene ultrananolites. Through transmission electron microtomography, however, we can see that most of the titanomagnetite crystals are distributed apart from the pyroxenes. This reveals that the titanomagnetite ultrananolite nucleated homogeneously (Supplemental Material 1).

Figure 10 shows a log-log plot of area number density divided by size intervals (n^*) for pyroxene and Fe–Ti oxide from 1 nm to 5.2 μm in the dense juvenile fragment. The size interval used for the n^* calculation is shown by the length of bars. Dividing by size interval makes it possible to compare the area number densities with different sizes. In Table 4, the appearance and n^* of pyroxene ultrananolite, titanomagnetite microlite and ultrananolite, and Fe-rich spots are summarized with respect to the three groups of erupted products. The raw data of the areal number densities of microlite and ultrananolite of Fe–Ti oxides are the same as those reported by Mujin and Nakamura (2014), although the results were recalculated for this reason. The number of 1–2 nm Fe-rich spots in the HAADF-STEM image (Fig. 9b) was measured for the thin section, throughout its thickness. The raw number density was thus overcounted compared to

289 that counted on the SEM images of polished surface. We therefore recalculated it by
290 assuming that the section thickness is 100–150 nm.

291 **Minimum crystal size and the smallest measurable number density.** In this
292 study, we observed minute spots down to 1 nm by utilizing TEM. The lattice parameters
293 of magnetite and augite are 0.8396 and 0.525–0.98 nm (Deer et al., 1992), respectively;
294 thus, this resolution is fairly close to the theoretically minimum nucleus radius of the
295 minerals. A drawback of such high-magnification observation is a narrowed field of
296 view, which results in high probability of undercounting the crystals. The relation
297 between size and n^* of the observable crystals was calculated as follows and is shown
298 in Figure 10. We obtained BSE images by SEM and HAADF-STEM at magnifications
299 of 50–100,000 and 1,500,000, respectively. At magnifications of 1,500,000, 100,000,
300 20,000, and 1,000, the fields of view were 94 × 100, 1,280 × 892, 6,400 × 4,460, and
301 1,280,000 × 89,200 nm, and the minimum measurable sizes of the crystals were 1, 5, 25,
302 and 500 nm when that is 5 pixels, respectively. The measurable maximum size was
303 regarded as the shorter (longitudinal) side length of field of view. The size interval to
304 obtain n^* from the area number density should be smaller than this maximum
305 measurable size. The theoretically smallest measurable number density per unit area
306 was obtained by dividing the unity by the counted area and then by the maximum size

interval, for example at a crystal size of 25 nm (2.5×10^{-5} mm) at magnification of 20,000, $n = 1/(6400\times4460)/(4460) \approx 7.9^{-12}$ nm^{-3} = 7.9^{6} mm^{-3}

Even if this constraint is considered, the gaps or hiatus in the size distribution still exist clearly for pyroxene and titanomagnetite. Another important finding is the presence of minimum crystal sizes except for the Fe-rich spots in the dense fragment. These crystals are ~100 nm for plagioclase in all samples and for pyroxene in the pumices of sub-Plinian and Vulcanian eruption, ~20 nm for pyroxene in a dense juvenile fragment, and a few hundred nanometers for Fe–Ti oxide in the pumices of sub-Plinian and Vulcanian eruption.

Morphology

Pyroxene microlite and nanolite with a width of 0.1–5.2 μm are generally acicular and often exhibit swallowtail, hopper, and hexagonal shapes in the polished sections. Hollow crystals are also common. These morphological characteristics indicate that the crystals grew rapidly under large undercooling. However, pyroxene ultrananolites on a diameter of 20–30 nm are spherical (Fig. 9 and Supplemental Material 1). The Fe–Ti oxide microlites and nanolite ≥~1 μm generally exhibit a euhedral rectangular shape, whereas ultrananolites (10–20 nm) of Fe–Ti oxide are spherical. It is noteworthy that pyroxene and Fe-Ti oxide ultrananolites are spherical.

Two possibilities are considered for the spherical shape. (1) The spherical shape is almost an equilibrium form, resulting from the lack of interfacial free energy anisotropy. It is known that in the case of ionic crystals, equilibrium form is accomplished rather than the growth form when crystal size is equal to or less than one micrometer at high temperatures where atoms move quickly to reduce interfacial energy (Heyraud and Métois, 1987). The anisotropy could be weakened either by the effect of thermal fluctuation at high temperature (Herring, 1951) or by losing the character of bulk crystal on less than a few nanometer scale crystals (e.g., Buffat and Borel, 1976). (2) The spherical shape is a growth form, not dominated by interfacial energy, because of crystal growth at very high undercooling (Welsch et al. 2014).

DISCUSSION

Mineralogical characteristics of pyroxene nanolite and ultrananolite

Contrary to the traditional petrographic view that rapidly grown groundmass pyroxenes are pigeonite, the space group of crystallographically composite pyroxene nanolites are partly sub-calcic augite and augite (*C*2/*c*) and orthopyroxene (*Pbca*) (Fig. 5). The pyroxene ultrananolites are ferroaugite (*C*2/*c*). The pyroxene compositions are not plotted on a single isotherm of Lindsley (1983) at 1 atm; instead, they are more or less in disequilibrium (Fig. 4). The augite crystals plot on the 1200 °C, while the

343 Ca-poor pyroxenes in contact with the augite crystals are orthopyroxene, not pigeonite,
344 indicating that the temperature should be lower than ~1100 °C. Under equilibrium, the
345 Ca-poor pyroxene becomes pigeonite at temperatures above 1100 °C. Growth of the
346 sub-calcic augite (*C*2/*c*) domain is assumed to have occurred, followed by the
347 crystallization of pyroxene ultrananolite. Sharp et al. (1996) also reported zoned
348 pyroxene nanolites with orthopyroxene cores and clinopyroxene rims, though their
349 samples contained pigeonite.

350 The pyroxene ultrananolites are Fe-rich compared to the sub-calcic augite
351 domain of nanolites by 9–14 mol % in ferrosilite content (Table 2, Fig. 4). This
352 deviation from equilibrium partitioning may be caused by a kinetic effect in rapid
353 growth. The Fe-enrichment of rapidly grown groundmass pyroxene was reported for
354 Apollo 12 Lunar basalts by Kushiro et al. (1972).

355 The pyroxene and titanomagnetite ultrananolites are both absent within
356 ~250–500 nm from the outer rim of pyroxene and magnetite nanolites (Fig. 7a). This
357 shows that the growth rates of the pyroxene and magnetite nanolites were rapid
358 enough to form diffusive boundary layers in which the iron was depleted. Similar
359 compositional boundary layers without ultrananolites were reported for glass-rich
360 andesitic tephra from Southern Taupo Volcanic Zone (Zellmer et al., 2016).

Crystallization processes of nanolites and ultrananolites

The primary mechanism by which effective undercooling (ΔT) is produced for microlites is assumed to be decompression-induced dehydration of hydrous magma (Cashman and Blundy, 2000). Here, we focus on the crystallization process of nanolites and ultrananolites. Below we examine the production of ΔT based on phase diagrams of simple systems. A primary characteristic of the nanolites and ultrananolites in the present study is their very large number density. A steepening CSD slope of decreasing size was observed through either primitive or high-level stereological corrections for pyroxenes and plagioclase, except for plagioclase in the sub-Plinian pumices. Such an increase in the nucleation rate was possibly caused by an increase of effective ΔT due to progressive degassing, in addition to hindered crystallization differentiation due to decreased diffusivity in the intercrystalline dehydrated melt.

Another major finding is the presence of practical minimum sizes and gap in size distribution. This indicates practical pause (freezing) of nucleation. The kinetics of nucleation and growth are then discussed.

Considerations on phase diagrams. Let us first consider the development of undercooling and crystallization volume with magma ascent on binary, ternary, and pseudoternary phase diagrams. First, we assumed a system saturated with a single

379 mineral phase (Fig. 11). If crystallization differentiation of the melt catches up with the
380 increase of the liquidus temperature by decompression, ΔT is not produced or does not
381 increase, as shown in the binary phase diagram (Fig. 11). Because the liquidus
382 temperature generally increases more rapidly with decreasing pressure (i.e., approaching
383 the surface), ΔT has the potential to increase rapidly even if the magma decompression
384 rate is constant (e.g., plagioclase: Bowen, 1913, and Yorder, 1957; diopside (Di)–
385 anorthite (An) system: Yoder et al., 1957, Yoder, 1965, and Weill et al., 1980a).

386 In multi-component systems, the changes in ΔT for constituting phases may
387 show complex behavior, depending on their relative increase of liquidus temperature
388 with decompression. Here, we consider the Di–An–albite (Ab) system as a
389 representative case. With decreasing water pressure, the liquidus volume of plagioclase
390 expands, and the cotectic boundary shifts toward Di (Fig. 12a). This results in a larger
391 increase in ΔT for the cotectic melt with respect to plagioclase than that for Di, which
392 explains the dominancy of plagioclase as a microlite phase of intermediate magmas.
393 The following plagioclase crystallization results in differentiation of melt and increase
394 in ΔT for Di (Fig. 12b). If the shift of the cotectic composition is significant, the initial
395 cotectic melt could even exceed the metastable liquidus of Di (Fig. 12c). In such a case,
396 crystallization of Di pauses until the melt composition returns to the metastable liquidus

by plagioclase crystallization (Fig. 12c).

In the orthpyroxene (Opx)–Plagioclase (Pl)–SiOr–Magnetite (Mag) pseudoternary system (e.g., Merzbacher and Eggler, 1984; Baker and Eggler, 1987), the liquidus volume of Pl expands, and the cotectic boundary between Opx and Pl shifts toward Opx with decreasing water pressure. This results in the "liquid line of pressure descent," where the compositional trace of melt is subject to decompression and fractional crystallization, in a direction nearly parallel to the Pl–SiOr line. This indicates that the crystallization volume of plagioclase becomes much larger than that of pyroxenes, which is consistent with the relative amount of ΔT between plagioclase and pyroxenes in the above Di–An–Ab system.

Because nanolite and ultrananolite crystallization may occur at a very low pressure, the effects of cooling and oxidation could also be important, in addition to decompression. The liquidus temperature of Fe–Ti oxides, among others, is strongly affected by oxygen fugacity (e.g., Toplis and Carroll, 1995). For example, the liquidus temperature of magnetite increases by 60 °C with increasing fO_2 by 2.0 log units from ΔQFM=-2.0 (quartz–fayalite–magnetite) at atmospheric pressure with a ferro-basalt composition.

Factors controlling nucleation rate. Next, we consider the theoretical aspects

of crystal nucleation that could have caused the slope change of CSD, occurrence of minimum sizes and gap in the size distribution. Generally, the nucleation rate is controlled by the activation energy of nucleation (ΔG^*), which is proportional to the cube of interfacial energy (σ) between the crystal and melt and inverse to the square of supersaturation ($\Delta\mu$). Dowty (1980) calculated the interfacial energy between alkali feldspar and $NaAlSi_3O_8$–$KAlSi_3O_8$–H_2O melt to be 0.015 J/m^2 at 9.5 wt% H_2O and 0.04 J/m^2 at 1.7 wt% H_2O at a confining pressure of 2.5 kbar. Hammer (2004) obtained the interfacial energy between feldspar and Pinatubo dacite melt based on single-step decompression experiments and the nucleation theory. The values increased systematically from 0.024 to 0.100 J/m^2 with a decrease in H_2O content from 4.8 to 0.8 wt%. Assuming nearly constant temperature, the interfacial energy may increase significantly in the intermediate–silicic melt under very low pressure.

The nucleation rate depends also on the melt diffusivity (e.g., Toramaru, 1991). Hammer and Rutherford (2002) showed in their single-step decompression crystallization experiments of dacitic melt that the nucleation rates of plagioclase dropped at very high effective ΔT, forming a bell-shaped nucleation rate against ΔT. They attributed the decrease in the nucleation rate to increased melt viscosity and decreased mobility of plagioclase-forming components owing to dehydration.

Origins of ultrananolite, minimum crystal size and gap in size distribution.

In the "transient nucleation" processes, the critical nucleation size is defined as a size above which the number of growing "subcritical clusters," either crystalline or amorphous, exceeds that of decaying ones (e.g., Kelton, 1995). The ultrananolite-sized particles observed in the quenched lithic fragment could be either stable crystals or subcritical clusters. The minimum crystal size may occur when groundmass crystallization enters the growth stage, i.e., when nucleation pauses (freezes) while growth continues. At this stage, the subcritical clusters should decay or be consumed (eaten) by the growing stable nuclei and become eventually unobservable. This is expected to occur when the critical nucleation size increases and the number flux of growing subcritical clusters decreases through a decrease of $\Delta\mu$ (ΔT), increase of σ, and decrease of diffusivity in the melt.

On the other hand, the gap in size distribution is assumed to have been formed when the decaying subcritical clusters are left quenched, or nucleation was resumed after the subcritical clusters had disappeared. Two gaps in the size distribution of Fe-Ti oxide cannot be explained by a single nucleation process; in this case, resumption of nucleation was required.

Kuo and Kirkpatrick (1982) reported that the critical nuclei radius of diopside

451 from the undercooled melt having a similar composition was determined with small
452 angle X-ray scattering (SAXS) to be 35–70 nm, when the undercooling (ΔT) was 10–
453 20 °C. We assume that the undercooling should have been larger in the samples in this
454 study, as shown in Figure 12a, and thus critical radius was smaller. Considering the
455 lattice constant of pyroxenes, we expect the critical nucleation radius to be larger than a
456 few nm. The ultrananolite-sized particle might, therefore, include subcritical clusters.

457 **ΔT change during eruption.** In volcanic eruptions, an accelerated increase in
458 ΔT may be caused by magma ascent and degassing in shallow conduits owing to the
459 nearly parabolic pressure dependence of water solubility in the melt, as discussed in
460 detail by Mollo and Hammer (2017). This explains the crystallization of high number
461 density nanolites. Thereafter, the ΔT may decrease with the progress of nanolite
462 crystallization. Together with an increase in σ and a decrease of diffusivity, decrease of
463 ΔT contributes to form minimum size. A situation that may produce large ΔT and enable
464 following resumption of ultrananolite crystallization includes rewelding of magma
465 spatters near the craters, i.e., formation of agglutinates (Sumner et al., 2005),
466 clastogenic (or rootless) lavas (e.g., Yasui and Koyaguchi, 2004), and tuffisites (Castro
467 et al., 2014). In these rocks, rapid decompression is followed by extensive dehydration
468 and possibly oxidation by fragmentation, whereas high temperature was maintained in

469 the interiors of the magma fragments.

470 ## IMPLICATIONS

471 ### Magma ascent processes of the 2011 Shinmoedake eruption

472 We observed groundmass crystals in a wide range of magnifications using
473 different electron microscopes such as W-SEM, FE-SEM, and TEM, and obtained the
474 semi-log CSDs of pyroxene and plagioclase at a size range of 0.1 μm–5.2 μm for the
475 three types of erupted materials (Fig. 3). In addition, we obtained the log-log size
476 distribution of pyroxenes and Fe–Ti oxides and Fe-rich spots at a size range of 1 nm–
477 5.2 μm for a dense juvenile lithic fragment from a Vulcanian explosion (Fig. 10). The
478 notable results obtained from these analyses are as follows. (1) The CSD slope of
479 plagioclase in sub-Plinian pumices did not increase with decreasing size, whereas those
480 in the Vulcanian pumices and dense juvenile fragments increased (Fig. 3). (2) In
481 contrast, the CSD slopes of pyroxene in all the erupted materials increased with
482 decreasing size. The CSDs did not change from sub-Plinian to Vulcanian pumices (Fig.
483 3). (3) The minimum crystal sizes were observed for all the minerals except for the
484 Fe-rich spots. The gaps in the size distribution were found for pyroxene and Fe–Ti
485 oxides in the size range of less than ~100 nm (Fig. 10). The observations in (1) and (2)
486 indicated that the timing of the increase of nucleation rate was earlier for pyroxene than

for plagioclase, and that the nucleation and growth of pyroxene is completed mostly before the increase of nucleation rate of plagioclase. This is consistent with observation (3), that the nucleation of pyroxene in the sub-Plinian pumice paused before eruption, resulting in the presence of minimum-sized crystals.

The shallow magmatic processes of the 2011 Shinmoedake eruption can be constrained from the above observations on groundmass crystallization as follows (Fig. 13). Observations (1) and (2) clearly imply that until the stage of pyroxene nanolite crystallization, the magma ascent rates were so similar as to be indistinguishable by crystallization between the sub-Plinian and lava extrusion-Vulcanian phases, and that magma fragmentation of the sub-Plinian eruption occurred before the increase of nucleation rate for plagioclase. Observation (3) suggests that some lithic fragments have a clastogenic origin. After welding, the magma continuously dehydrated, and plagioclase nucleation rate may have increased, leading to the resumption of pyroxene and Fe–Ti oxide ultrananolite crystallization. In the lava extrusion-Vulcanian phase, magma fragmentation occurred after the increase of nucleation rate for plagioclase. The emplacement processes of the non-clastogenic effusive lava and magma erupted as Vulcanian pumice were so similar as to be indistinguishable from the groundmass crystallization. By experimentally determining the crystallization conditions of (ultra)

505 nanolites, such as pressure, temperature, duration, and fO_2, the depth and timing that
506 controlled the eruption style transition can be constrained.

507 **ACKNOWLEDGMENTS**

508 The authors thank Shin Ozawa and Yohei Igami for technical assistance in the FIB
509 processing of TEM samples. The authors also benefitted from the thoughtful comments
510 by Shugo Ohi on the phase relation of pyroxene and discussions with Satoshi Okumura.
511 The official reviews by Alexander Simakin, Julia Hammer and Michael Higgins greatly
512 improved the manuscript. This work was supported by JSPS KAKENHI Grant Numbers
513 JP262753 to MM and JP25287141 and JP16H06348 to MN. The tuition fees of MM
514 were supported by a Grant-in-Aid of Tohoku University Institute for Promoting
515 Graduate Degree Programs Division for Interdisciplinary Advanced Research and
516 Education.

517 **REFERENCE CITED**

518 Baker, D.R., and Eggler, D.H. (1987) Compositions of anhydrous and hydrous melts
519 coexisting with plagioclase, augite, and olivine or low-Ca pyroxene from 1 atm to 8
520 kbar; application to the Aleutian volcanic center of Atka. American Mineralogist, 72,
521 12–28.

522 Bowen, N.L. (1913) The melting phenomena of the plagioclase feldspars. American

Journal of Science, 210, 577–599.

Buffat, P., and Borel, J. P. (1976) Size effect on the melting temperature of gold particles. Physical Review A, 13, 2287–2298.

Cashman, K.V. (1992) Groundmass crystallization of Mount St. Helens dacite, 1980–1986: a tool for interpreting shallow magmatic processes. Contributions to Mineralogy and Petrology, 109, 431–449.

Cashman, K.V. and Blundy, J. (2000) Degassing and crystallization of ascending andesite and dasite. Philosophical Transactions of the Royal Society of London A: Mathematical, Physical and Engineering Sciences, 358, 1487–1513.

Castro, J.M., Cashman, K.V and Manga, M. (2003) A technique for mesuaring 3D crystal-size distributions of prismatic microlites in obsidian, American Mineralogist, 88, 1230–1240.

Castro, J.M., Bindeman, I.N., Tuffen, H., and Schipper, C.I. (2014) Explosive origin of silicic lava: textural and δD–H_2O evidence for pyroclastic degassing during rhyolite effusion. Earth and Planetary Science Letters, 405, 52–61.

Deer, W.A., Howie, R.A., and Zussman, J. (1992) An introduction to the Rock-forming minerals 2nd ed., p. 177 and p. 558. Prentice Hall.

Dowty, E. (1980) Crystal growth and nucleation theory and the numerical simulation of

igneous crystallization. In R.B. Hargraves, Ed., Physics of magmatic processes, p. 419–485. Princeton University Press, Princeton, NJ.

Eggler, D.H., and Burnham, C.W. (1984) Solution of H_2O in diopside melts: A thermodynamic model. Contributions to Mineralogy and Petrology, 85, 58–66.

Geospatial Information Authority of Japan (GSI), GSI Maps: http://maps.gsi.go.jp/, accessed April, 2014.

Hammer, J.E. (2004) Crystal nucleation in hydrous rhyolite: Experimental data applied to classical theory. American Mineralogist, 89, 1673–1679.

Hammer, J.E., and Rutherford, M.J. (2002) An experimental study of the kinetics of decompression□induced crystallization in silicic melt. Journal of Geophysical Research, 197, 1–23.

Herring, C. (1951) Some theorems on the free energies of crystal surfaces. Physical Review, 82, 87–93.

Heyraud, J.C., and Métois, J.J. (1987) Equilibrium shape of an ionic crystal in equilibrium with its vapour (NaCl). Journal of crystal growth, 84, 503–508.

Higgins, M.D. (2000) Measurement of crystal size distributions. American Mineralogist, 85, 1105–1116.

Japan Coast Guard (JCG) Hydrographic and Oceanographic Department:

559 http://www1.kaiho.mlit.go.jp/jishin/sokuryo/sokuryo.html accessed April, 2014.

560 Japan Meteorological Agency (JMA) (2011) Volcanic Activity Documents of

561 Kirishimayama volcano (in Japanese):

562 http://www.data.jma.go.jp/svd/vois/data/tokyo/STOCK/monthly_v-act_doc/monthly

563 _vact_505.html, accessed Dec. 01. 2016.

564 Japan Meteorological Agency (JMA) (2012) Volcanic activity of Kirishimayama

565 Volcano –February, 2011 – May, 2011–, Report of Coordinating Committee for

566 Prediction of Volcanic Eruption, 109, 139–167 (in Japanese).

567 Japan Meteorological Agency (JMA) (2016) National Catalogue of the Active

568 Volcanoes in Japan (The fourth edition, English version):

569 http://www.data.jma.go.jp/svd/vois/data/tokyo/STOCK/souran_eng/menu.htm,

570 accessed Oct. 08, 2016.

571 Johannsen, A. (1931) A Descriptive Petrography of the Igneous Rocks, v. 1, p. 37. The

572 University of Chicago Press, Chicago, Illinois.

573 Johannes, W. (1978) Melting of plagioclase in the system Ab−An−H_2O and

574 Qz−Ab−An− H_2O at P_{H2O} = 5 kbars, an equilibrium problem. Contributions to

575 Mineralogy and Petrology, 66, 295–303.

576 Kamada, T., MapMap ver.6.0, A blank map:

http://www5b.biglobe.ne.jp/t-kamada/CBuilder/mapmap.htm, accessed April, 2014.

Kelton, K.F. (1995) Transient nucleation in glasses. Materials Science and Engineering: B, 32, 145–152.

Kozono, T., Ueda, H., Ozawa, T., Koyaguchi, T., Fujita, E., Tomiya, A., and Suzuki, Y.J. (2013) Magma discharge variations during the 2011 eruptions of Shinmoe-dake volcano, Japan, revealed by geodetic and satellite observations. Bulletin of Volcanology, 75, 695–707.

Kuo, L.C., and Kirkpatrick, R.J. (1982) Small angle X-ray scattering study of pre-nucleation behavior of titanium-free and titanium-bearing diopside glasses. American Mineralogist, 67, 676–685.

Kushiro, I., Nakamura, Y., Kitayama, K., and Akimoto, S. (1971) Petrology of some Apollo 12 crystalline rocks. Proceedings of the Second Lunar Science Conference, 1, 481–495.

Lindsley, D.H. (1983) Pyroxene thermometry. American Mineralogist, 68, 477–493.

Merzbacher, C., and Eggler, D.H. (1984) A magmatic geohygrometer: application to Mount St. Helens and other dacitic magmas. Geology, 12, 587–590.

Miyabuchi, Y., Hanada, D., Niimi, H., and Kobayashi, T. (2013) Stratigraphy, grain-size and component characteristics of the 2011 Shinmoedake eruption deposits,

595 Kirishima Volcano, Japan. Journal of Volcanology and Geothermal Research, 258,
596 31–46.
597 Mollo, S., and Hammer, J.E. (2017) Dynamic crystallization in magmas. EMU Notes in
598 Mineralogy, 16, 373–418.
599 Morgan, D.J., and Jerram, D.A. (2006) On estimating crystal shape for crystal size
600 distribution analysis. Journal of Volcanology and Geothermal Research, 154, 1–7.
601 Mujin, M., and Nakamura, M. (2014) A nanolite record of eruption style transion.
602 Geology, 42, 661–614.
603 Nakada, S., Nagai, M., Kaneko, T., Suzuki, Y., and Maeno, F. (2013) The outline of the
604 2011 eruption at Shinmoe-dake (Kirishima), Japan. Earth, Planets and Space, 65,
605 475–488.
606 Nakamura, M., and Shimakita, S. (1998) Dissolution origin and syn-entrapment
607 compositional change of melt inclusion in plagioclase. Earth and Planetary Science
608 Letters, 161, 119–133.
609 Ozawa, T., and Kozono, T. (2013) Temporal variation of the Shinmoe-dake crater in the
610 2011 eruption revealed by spaceborne SAR observations. Earth, Planets and Space,
611 65, 527–537.
612 Paulick, H., and Franz, G. (1997) The color of pumice: case study on a trachytic fall

613 deposit, Meidob volcanic field, Sudan. Bulletin of Volcanology, 59, 171–185.

614 Perchuk, L.L., Kushiro, I., and Kosyakov, A.V. (1988) Exprimental determination of
615 the liquidus surface in the system diopside-water. Geokhimiya, 7, 942–955 (not seen;
616 extracted from Perchuk, L.L., and Kushiro, I. (1991) Thermodynamics of the
617 Liquidus in the System Diopside–Water: A Review. In L.L. Perchuk and I. Kushiro,
618 Eds., Physical Chemistry of Magmas, p. 249–267. Springer-Verlag, New York).

619 Reed, W. P. (1993) Certificate of analysis for standard reference material 2063a.
620 National Institute of Standards and Technology, Gaithersburg, MD, 20899.

621 Schlinger, C.M., Smith, R.M., and Veblen, D.R. (1986) Geologic origin of magnetic
622 volcanic glasses in the KBS tuff. Geology, 14, 959–962.

623 Schlinger, C.M., Rosenbaum, J.G., and Veblen, D.R. (1988) Fe-oxide microcrystals in
624 welded tuff from southern Nevada: Origin of remanence carriers by precipitation in
625 volcanic glass. Geology, 16, 556–519.

626 Sharp, T.G., Stevenson, R.J., and Dingwell, D.B. (1996) Microlites and “nanolites” in
627 rhyolitic glass: microstructural and chemical characterization. Bulletin of
628 Volcanology, 57, 631–640.

629 Shimbori, T., Sakurai, T., Tahara, M., and Fukui, K. (2013) Observation of Eruption
630 clouds with weather radars and meteorological satellite: a case study of the eruption

631 at Shinmoedake volcano in 2011. Quarterly Journal of Seismology, 77, 139–214.

632 Sumner, J.M., Blake, S., Matela, R.J. and Wolff, J.A. (2005) Spatter. Journal of

633 Volcanology and Geothermal Research, 142, 49–65.

634 Suzuki, Y., Yasuda, A., Hokanishi, N., Kaneko, T., Nakada, S., and Fujii, T. (2013)

635 Syneruptive deep magma transfer and shallow magma remobilization during the

636 2011 eruption of Shinmoe-dake, Japan-Constraints from melt inclusions and phase

637 equilibria experiments, Journal of Volcanology and Geothermal Research, 257, 184–

638 204.

639 Toramaru, A. (1991) Model of nucleation and growth of crystals in cooling magmas.

640 Contributions to Mineralogy and Petrology, 108, 106–117.

641 Toplis, M.J., and Carroll, M.R. (1995) An experimental study of the influence of

642 oxygen fugacity on Fe-Ti Oxide stability, phase relations, and mineral-melt

643 equilibria in ferro-basaltic systems. Journal of Petrology, 36, 1137–1170.

644 The national institute of advanced industrial science and technology (AIST), Geological

645 map display system of Geological Survey of Japan, GeomapNavi,

646 https://gbank.gsj.jp/geonavi/?lang=en, accessed October, 2016.

647 Wager, L.R. (1961) A note on the origin of ophitic texture in the chilled olivine gabbro

648 of the Skaergaard intrusion. Geological Magazine, 98, 353–364.

649 Watanabe, M., and Williams, D.B. (2006) The quantitative analysis of thin specimens: a
650 review of progress from the Cliff-Lorimer to the new ζ-factor methods. Journal of
651 Microscopy, 221, 89–109.
652 Weill, D.F., Stebbins, J.F., Hon, R., and Carmichael, I.S.E. (1980a) The enthalpy of
653 fusion of anorthite. Contributions to Mineralogy and Petrology, 74, 95–102.
654 Weill, D.F., Hon, R., and Navrotsky, A. (1980b) The igneous system
655 CaMgSi2O6-CaAl2Si2O8-NaAlSi3O8: variations on a classic theme by Bowen. In
656 R.B. Hargraves, Ed., Physics of Magmatic Processes, p. 49–92. Princeton University
657 Press, Princeton, NJ.
658 Welsch, B., Hammer, J., and Hellebrand, E. (2014) Phosphorus zoning reveals dendritic
659 architecture of olivine. Geology, 42, 867–870.
660 Yasui, M., and Koyaguchi, T. (2004) Sequence and eruptive style of the 1783 eruption
661 of Asama Volcano, central Japan: a case study of an andesitic explosive eruption
662 generating fountain-fed lava flow, pumice fall, scoria flow and forming a cone.
663 Bulletin of Volcanology, 66, 243–262.
664 Yoder, H.S., Stewart, D.B., and Smith, J.R. (1957) Ternary feldspars. Carnegie
665 Institution of Washington Year book, 56, 206–214.
666 Yoder, H.S. (1965) Diopside-anorthite-water at five and ten kilobars and its bearing on

667 explosive volcanism. Carnegie Institution of Washington Year book, 64, 82–89.
668 Zellmer, G.F., Sakamoto, N., Hwang, S.L., Matsuda, N., Iizuka, Y., Moebis, A., and
669 Yurimoto, H. (2016) Inferring the Effects of Compositional Boundary Layers on
670 Crystal Nucleation, Growth Textures, and Mineral Chemistry in Natural Volcanic
671 Tephras through Submicron-Resolution Imaging. Frontiers in Earth Science, 4, 88.
672 Ziegler, D., and Navrotsky, A. (1986) Direct measurement of the enthalpy of fusion of
673 diopside. Geochimica et Cosmochimica Acta, 50, 2461–2466.

674 **LIST OF FIGURE CAPTIONS**

675 **Figure 1. (a)** Location and **(b)** contour maps of the Kirishima volcano group. The
676 coastlines and counters were drawn by MapMap software (version 6.0) and GSI Maps
677 of the Geospatial Information Authority of Japan, respectively. The active volcano and
678 caldera information in this region was obtained from the National Catalogue of the
679 Active Volcanoes in Japan (Fourth Edition, Japan Meteorological Agency), and location
680 of the Nankai trough was obtained from a bathymetric chart of the Japan Coast Guard.
681 The craters of the Kirishima volcano group were determined from GeomapNavi,
682 Geological map display system of Geological Survey of Japan, National Institute of
683 Advanced Industrial Science and Technology. **(c)** Top surface of the sampling location
684 (Takachihogawara). The well-preserved nature of original deposition was confirmed by

685 jigsaw impact cracks. The scale is in cm.

686 **Figure 2.** Backscattered electron (BSE) images of groundmass of the pyroclasts from
687 the Shinmoedake 2011 eruption. **(a) and (b)**: gray pumice of the sub-Plinian eruption;
688 **(c) and (d)**: gray pumice of the Vulcanian explosion; and **(e) and (f)**: dense juvenile
689 fragment from the Vulcanian explosions. Abbreviations: Pl, plagioclase; Pyx, pyroxene;
690 Ox, Fe–Ti oxides.

691 **Figure 3.** Semi-log crystal size distribution (CSD) plots for pyroxene (Pyx; upper row)
692 and plagioclase (Pl; lower row). The crystal width (shorter side of rectangle) measured
693 in back scattered electron images are used as the crystal size. CSDCorrections (Higgins,
694 2000) was applied to the raw data of Mujin and Nakamura (2014). The used data are
695 crystals from 0.1 to 5.2 μm in width before CSDCorrections is applied. We loaded two
696 separate data sets obtained from scanning electron microscopy with a tungsten filament
697 (W-SEM) and field emission (FE-SEM) to CSDCorrections. The total number of
698 measurements are shown in each panel. **(a) and (b)**: pumices of the sub-Plinian
699 eruptions; **(c) and (d)**: pumices of the Vulcanian explosions; **(e) and (f)**: dense juvenile
700 fragments of the Vulcanian explosions.

701 **Figure 4.** Chemical compositions of pyroxene in the dense juvenile fragment of the
702 Vulcanian explosion. The nanolite crystals (~1 μm) have a composite structure

consisting of at least three domains. Each crystal is represented by different symbols (circle, triangle, and cross). The bright field-transmission electron microscopy (BF-TEM) image and the analyzed points of crystal A (circle) are shown in Figure 5. The sizes of ultrananolites analyzed with TEM (x-mark) were ~20–30 nm on a diameter. The polythermal isopleths represent equilibrium pyroxene compositions from Lindsley (1983).

Figure 5. (a) High-angle annular dark-field scanning transmission electron microscopy (HAADF-STEM) image and **(b–e)** X-ray intensity maps of Al, Fe, Mg, and Ca respectively, for the same area of a pyroxene nanolite in the dense juvenile fragment. **(g–i)** The selected area diffraction (SAD) patterns obtained from the points x, y, and z in the BF-TEM image **(f)**. On the basis of the chemical compositions and SAD patterns, the phases were determined to be orthopyroxene (Opx, *Pbca*) for **(g)**, Ca-rich augite (Aug, *C*2/*c*) for **(h)** and sub-calcic augite (*C*2/*c*) for **(i)** with the electron beam along with $[10\bar{5}]$, $[10\bar{2}]$, and $[10\bar{2}]$ zone axes, respectively. Concentric compositional zoning is observed in **(a–d)**.

Figure 6. (a) BF-TEM image of the dense juvenile fragment. **(b–d)** The SAD patterns of pyroxene ultrananolites in **(a)**. On the assumption that these crystals have the same crystallographic structure, the diffraction patterns correspond to the *C*2/*c* clinopyroxene

721 structure with the electron beam along the **(b)** [$\bar{1}12$], **(c)** [013], and **(d)** [$1\bar{3}\bar{2}$] or [103]

722 zone axes.

723 **Figure 7. (a) and (b)** BF-TEM images of a dense juvenile fragment with relatively

724 lower and higher magnifications, respectively. Tiny crystals <30 nm on a diameter are

725 absent within ~250–500 nm from the outer rim of pyroxene (Pyx) and titanomagnetite

726 (arrow) with a width of ~0.5–1 μm in **(a)**. **(c)** SAD pattern of titanomagnetite indicated

727 by the arrow in **(a)**, showing a twin structure corresponding to the [$1\bar{1}0$] zone axis of

728 the *Fd*$\bar{3}$*m* structure. **(d)** Fourier transform of a titanomagnetite ultrananolite shown by

729 the arrow in **(b)** corresponding to [$0\bar{1}1$] zone axis of the *Fd*$\bar{3}$*m* structure.

730 **Figure 8. (a)** HAADF-STEM image and **(b–f)** X-ray intensity maps of Fe, Ti, Si, Mg,

731 and Ca, respectively, in a dense juvenile fragment. The brighter dots in the

732 HAADF-STEM image are titanomagnetite (Ox), which correspond to the brighter dots

733 in the X-ray intensity maps of Fe and Ti. Abbreviation: Pyx, pyroxene.

734 **Figure 9. (a)** BSE image and **(b)** HAADF-STEM image of a Vulcanian dense juvenile

735 fragment. This fragment, among the five observed fragments includes pyroxene (Pyx)

736 ultrananolites <30 nm on a diameter and Fe–Ti oxide (Ox) ultrananolites <20 nm and

737 Fe-rich spots <2 nm. Abbreviation: UN, ultrananolite.

738 **Figure 10.** Log-log plot of crystal number density per unit area (m^{-2}) at a given size

739 (width) interval (n* m^{-3}) versus crystal size for pyroxene and Fe–Ti oxide in the dense
740 juvenile fragment. The used data are crystals from 1 nm to 5.2 μm. Data for pyroxene
741 and Fe–Ti oxides are shown by solid and dotted horizontal bars, respectively. Note that
742 crystal size intervals are different for each crystal size, which are shown by the length of
743 the bars (pyroxene: 300 nm interval for <0.1–5.2 μm crystals, 10 nm for 20–30 nm;
744 Fe-Ti oxides: 4 μm for 1–5 μm, 10 nm for 10–20 nm, Fe-rich spots: 1 nm for 1–2 nm).
745 Note that because the Fe-rich spots (*) were observed through the thin sections in
746 HAADF-STEM image, their number density was recalculated into the value of 2D
747 section by assuming the section thickness to be 100 –150 nm. The double-arrowed bars
748 represent measurable ranges of crystal size and the lower limit of the crystal number
749 density measureable at the magnification shown. The number density in the shaded area
750 may be undercounted in a single microscopic view at each magnification. The dashed
751 lines at the bottom represent the microscopy applied to the size ranges: TEM, FE-SEM,
752 and W-SEM, respectively.
753 **Figure 11.** Schematic illustrations of the development of undercooling (ΔT) and
754 evolution of melt composition with decompression of volatile-saturated magma on a
755 binary phase diagram of plagioclase. The solidus lines are from Johannes (1978; 500
756 MPa, H_2O saturated) and Bowen (1913; 1 atm, dry). The liquidus lines are from Yoder

(1957; 500 MPa, H_2O saturated) and Bowen (1913; 1 atm, dry). We complemented the solidus and liquidus lines except for 500 MPa and 1 atm. **(a)** If crystallization differentiation of melt catches up with the increase in the liquidus temperature by decompression, ΔT is kept constant. **(b)** If the liquidus temperature increase accelerates with decreasing pressure (i.e., approaching the surface), ΔT may further increase. Note that the illustrated temperature does not correspond to that of Shinmoedake magma.

Figure 12. (a) Schematic illustrations of the development of undercooling (ΔT) and evolution of melt composition with magma decompression in the diopside (Di)–anorthite (An)–albite (Ab) ternary phase diagram. The cotectic lines are from Weill et al. (1980b; 1 atm, dry), Nakamura and Shimakita (1998; 200 MPa, H_2O saturated), and Yoder (1965; 500 MPa, H_2O saturated). The An liquidus temperatures are from Weill et al. (1980a; 1 bar, dry), Yoder (1957; 200 MPa, H_2O saturated), and Yoder (1965; 500 MPa and 1 GPa, H_2O saturated). The Di liquidus temperatures are from Ziegler and Navrotsky (1986; 1 bar, dry), Eggler and Burnham (1984; 200 MPa, H_2O saturated), Yoder (1965; 500 MPa, H_2O saturated), and Perchuk et al. (1988; 1 GPa, H_2O saturated). The Di–An eutectic point at 1 GPa is from Yoder (1965). **(b)** With decreasing water pressure, the liquidus volume of the plagioclase expands, and the cotectic composition shifts toward Di. This results in a larger increase in ΔT for the

775 initial cotectic melt with respect to plagioclase than that with respect to Di. The
776 following plagioclase crystallization causes differentiation of melt and increased ΔT for
777 Di. **(c)** If decompression and the resulting shift in the cotectic composition are
778 significant, the initial cotectic melt may be above the metastable liquidus of Di. In such
779 a case, the crystallization of Di is suspended until the melt composition returns to the
780 metastable liquidus through plagioclase crystallization.

781 **Figure 13.** Schematic illustration of crystallization sequences and timings of
782 groundmass crystals and their relationship with magma ascent and fragmentation during
783 the Shinmoedake 2011 eruption. The pressure–time path and timing of the
784 fragmentation of the magmas that caused the sub-Plinian eruption are shown in blue;
785 those for the Vulcanian eruption are shown in green. Two origins are assumed for the
786 dense juvenile fragments from the Vulcanian explosions (red). Some pumice clasts
787 likely fell from the sub-Plinian eruption column back into the crater and were welded at
788 relatively oxidized conditions to form ultrananolites of pyroxene and Fe–Ti oxides. The
789 other type of dense fragment, which is free of ultrananolites, is assumed to have been
790 part of extrusion lava. The dotted and solid bars at the bottom and left parts of the
791 diagram represent durations of nucleation and growth of the crystals, respectively. The
792 dashed part represents the period in which the growth was so small that the CSDs

practically did not change. The transit time of the Vulcanian magmas in the shallow conduit was longer than that of the sub-Plinian magma. The nucleation practically paused (froze) to some degree before the magma quenching for all minerals in all styles of eruption except for the Fe–rich spots. Compared with plagioclase, the increase of nucleation rate for pyroxene was formed earlier, and the nucleation of pyroxene practically paused (froze) earlier. Abbreviations: Pyx, pyroxene; Pl, plagioclase; Mag, magnetite; UN, ultrananolite; Nano, increase of nucleation rate of nanolite.

Supplemental material 1. Transmission electron microtomography (TEMT) of high-angle annular dark-field scanning transmission electron microscopy (HAADF-STEM) of pyroxenes (lower brightness) and possibly Fe–Ti oxide (higher brightness) in a dense juvenile fragment showing homogeneous nucleation of Fe–Ti oxide ultrananolites.

APPENDIX

Geophysical constraints on the magma ascent processes of the 2011 Shinmoedake eruption

Based on precise geodetic observations of volcanic edifice deflation with tilt meters and synthetic aperture radar (SAR) and of weather radar observations of the eruption cloud heights, the deflation of the magma chamber was detected synchronously at the formation time of the eruption column. This reveals that the sub-Plinian eruptions and lava extrusion were accompanied by simultaneous and continuous magma supplied from the magma chamber through an open conduit with direct connection to the surface. The following lava effusion that began 36 h after the last sub-Plinian eruption was also accompanied by deflation of the magma chamber. However, the Vulcanian explosions were not accompanied by magma chamber deflation, which indicates that the eruption was caused by the rupture of a pressurized shallow conduit and was not followed by magma migration from the chamber (Kozono et al., 2013; Kozono et al., 2014). The erupted volume and discharge rate during the sub-Plinian eruptions and lava extrusion were estimated to be 3.04–6.67 × 10^6 m^3 and 450–741 m^3/s and 12.1–15.1 × 10^6 m^3 and 70.0–87.4 m^3/s, respectively (Kozono et al., 2013). It should be noted that these discharge rates are within one order of magnitude, although the mode of eruption is

824 quite different. This is consistent with the observation of the eruption changing from
825 sub-Plinian eruption to lava effusion without a long pause. Assuming the conduit radius
826 is 5 m (Sato et al., 2013), the magma ascent rate for the sub-Plinian eruptions was
827 calculated to be 5.7–9.4 m/s, whereas that for the lava extrusion was 0.89–1.1 m/s; the
828 latter is one fifth to one ninth of the former. Based on the one-dimensional steady flow
829 model, Tanaka and Hashimoto (2013) estimated the magma fragmentation pressure to
830 be about 10 MPa.

831 **Semi-log CSD plots and the 2D raw data**

832 Here we used CSDCorrections version 1.54 (Higgins, 2000) to convert 2D
833 measurements of the short axis of the best-fitting box to 3D crystal size distributions on
834 a vesicle-free basis. Utilizing CSDCorrections requires estimation of the sample fabric
835 and grain roundness, in addition to the 3D crystal shape. Samples were assumed to be
836 free of fabric. Based on visual inspection of the samples, a roundness factor of 0.4 for
837 pyroxene and 0.2 for plagioclase were chosen. The 3D shapes of crystals were
838 determined using CSDSlice version 5 (Morgan and Jerram, 2006). The 3D crystal
839 shapes of pyroxene were mostly acicular (1.0:1.0–2.3:7.0–10) and that of all plagioclase
840 were rectangular prisms (1.0:3.4–5.0:10). The 2D raw data obtained separately from
841 W-SEM (low magnification; LM) and FE-SEM (high magnification; HM) were loaded

842 to CSDCorrections to produce single line. In order to compare the data among different
843 eruption styles, we used a common crystal shapes of 1:1:8 for pyroxene and 1:5:10 for
844 plagioclase, respectively, and number of bin/decade of 5 for both minerals.

845 Semi-log CSD plots from 0.1 μm to 5.2 μm in width shown in Figure S2 are
846 the revised versions of those reported by Mujin and Nakamura (2014) using the simple
847 method of Wager (1961). It should be noted that Wager (1961)'s conversion method
848 does not have a good theoretical basis and does not give accurate results (Higgins,
849 2000). The raw data are the same as those in Mujin and Nakamura (2014) and these are
850 shown in the crystal width frequency histograms (Fig. S1). Here, we obtained the
851 crystal number density (N) with the following equation:

852 $$N \text{ (in m}^{-4}\text{)} = (\text{number of crystals per analyzed area})^{1.5}/\text{length interval} \quad (1)$$

853 In the preceding paper, the value was calculated by (number of crystals per analyzed
854 area/length interval)$^{1.5}$, which gave higher N values in m$^{-4.5}$. The length interval was set
855 at 300 nm in all calculations, which enabled comparison of the CSD plots in this paper.
856 As found previously, the CSD plots of pyroxene and plagioclase exhibited a kink at
857 crystal widths of 2.0–2.7 μm for all erupted materials except for the plagioclase in the
858 sub-Plinian pumices. The plagioclase in the sub-Plinian pumices produced an almost
859 constant CSD slope down to a size of 400 nm. The semi-log CSDs parameters (the

values of intercept, $\ln N_0$, and slope -1/a) are shown in Table S1.

TABLE S1. Parameters for semi-log crystal size distribution (CSD) of plagioclase and pyroxene

		Sub-Plinian pumice			Vulcanian pumice			Vulcanian dense juvenile fragment		
	Size range	kink size (μm)	N_0[a] (mm^{-4})	a[b]	kink size (μm)	N_0[a] (mm^{-4})	a[b]	kink size (μm)	N_0[a] (mm^{-4})	a[b]
Pyroxene	**> kink size**	2.1	8.3×10^{8}	0.66	2.0	1.2×10^{9}	0.57	2.1	3.4×10^{8}	0.76
	< kink size		7.3×10^{10}	0.27		6.4×10^{10}	0.27		1.3×10^{11}	0.24
Plagioclase	**> kink size**	-	$1.9–5.3\times10^{8}$	0.81–1.06	2.7	3.5×10^{8}	0.93	2.2	2.0×10^{8}	1.08
	< kink size		-			6.2×10^{9}	0.47		5.2×10^{9}	0.42

Notes: The length interval was set to be 300 nm in all the calculation. (a) N_0: the number density of nuclei (cm^{-4}), calculated from the nucleation density per unit volume for crystals larger (>) and smaller (<) than the kink size obtained by CSD regression analyses (the vertical-axis intercept of the semi-log CSD plot; Figure S2). (b) a: the denominator of the CSD slope (-1/a). No kink was observed in the plagioclase of sub-Plinian pumices.

References (Appendix)

Higgins, M.D. (2000) Measurement of crystal size distributions. American Mineralogist, 85, 1105–1116.

Kozono, T., Ueda, H., Shinmbori, T., and Fukui, K. (2014) Correlation between magma chamber deflation and eruption cloud height during the 2011 Shinmoe-dake eruptions. Earth, Planets and Space, 66, 139–147.

Kozono, T., Ueda, H., Ozawa, T., Koyaguchi, T., Fujita, E., Tomiya, A., and Suzuki, Y.J. (2013) Magma discharge variations during the 2011 eruptions of Shinmoe-dake volcano, Japan, revealed by geodetic and satellite observations. Bulletin of Volcanology, 75, 695–707.

873 Morgan, D.J., and Jerram, D.A. (2006) On estimating crystal shape for crystal size
874 distribution analysis. Journal of Volcanology and Geothermal Research, 154, 1–7.
875 Mujin, M., and Nakamura, M. (2014) A nanolite record of eruption style transion.
876 Geology, 42, 661–614.
877 Sato, H., Suzuki-Kamata, K., Sato, E., Sano, K., Wada, K., and Imura, R. (2013)
878 Viscosity of andesitic lava and its implications for possible drain-back processes in
879 the 2011 eruption of Shinmoedake volcano, Japan. Earth Planets Space, 65, 623–631.
880 Tanaka, R., and Hashimoto, T. (2013) Transition in eruption style during the 2011
881 eruption of Shinmoe-dake, in the Kirishima volcanic group: Implications from a
882 steady conduit flow model. Earth, Planets and Space, 65, 645–655.
883 Wager, L.R. (1961) A note on the origin of ophitic texture in the chilled olivine gabbro
884 of the Skaergaard intrusion. Geological Magazine, 98, 353–364.

885 **Figure Captions (Appendix)**

886 **Figure S1.** Frequency histograms of crystal width in the size range of 0.1–5.2 μm for
887 sub-Plinian pumices **(a–d)**, Vulcanian pumices **(e–h)**, and dense juvenile fragments **(i–l)**,
888 obtained from back-scattered electron images taken with a field emission scanning
889 electron microscope (FE-SEM) at a magnification of ×5000 **(a, c, e, g, i, and k)** and
890 with an SEM with a tungsten filament (W-SEM) at a magnification of ×1000 **(b, d, f, h,**

j, and l). Each panel includes the total number of crystals measured in the size range of 0.1–5.2 μm and the size bin. Figures in parentheses are the total number of crystals including those larger than 5.2 μm. Cumulative relative frequency is shown in each panel.

Figure S2. Semi-log crystal size distribution (CSD) plots for pyroxene (Pyx; upper row) and plagioclase (Pl; lower row) in the size range of 0.1–5.2 μm. Here, the number densities per unit volume (N m^{-4}) were obtained by raising the number of crystals per unit area to the 3/2 power and dividing it by the size interval. The size interval is 300 nm for all panels. **(a) and (b)**: pumices of the sub-Plinian eruptions; **(c) and (d)**: pumices of the Vulcanian explosions; **(e) and (f)**: dense juvenile fragments of the Vulcanian explosions. The data were fitted with two straight lines, which are shown by solid and dotted lines with the least error sum of squares (R^2). The width and N at the junction of the two fitting lines are shown. Open and solid circles represent data obtained using scanning electron microscopy with a tungsten filament (W-SEM) and field emission (FE-SEM), respectively.

This is a preprint, the final version is subject to change, of the American Mineralogist (MSA)
Cite as Authors (Year) Title. American Mineralogist, in press.
(DOI will not work until issue is live.) DOI: http://dx.doi.org/10.2138/am-2017-6052CCBYNCND

907

TABLES

TABLE 1. Parameters for utilizing of CSDCorrections

Phase	Eruption style	Magni-fication[a]	Crystal shape parameters from CSDSlice				Analyzed area except for vesicles	Roundness	Vesicle	Size scale length Number of bins per decade [b]
			x	y	z	R^2	(μm^2)		(area %)	
pyroxene	Sub-Plinian pumices	high	1.0	1.0	8.0	0.7140	24753	0.4	0.0	5
		low	1.0	2.1	7.0	0.7715	66716			
	Vulcanian pumices	high	1.0	1.2	10.0	0.6533	7026			
		low	1.0	2.1	10.0	0.7315	76836			
	Lithic fragments	high	1.0	1.1	8.0	0.6933	5263			
		low	1.0	2.3	9.0	0.7262	57349			
plagioclase	Sub-Plinian pumices	high	1.0	5.0	10.0	0.8588	24753	0.2	0.0	5
		low	1.0	4.5	10.0	0.6622	66716			
	Vulcanian pumices	high	1.0	3.4	10.0	0.4933	7026			
		low	1.0	4.0	10.0	0.6993	76836			
	Lithic fragments	high	1.0	4.0	10.0	0.6063	5263			
		low	1.0	5.0	10.0	0.6891	57349			

Notes: (a) high and low represent the magnifications of BSE images at which the data were obtained (high: ×5000 with FE-SEM; low: ×1000 with W-SEM). The used data for high and low magnifications are from 0.1 to 5.2 μm and from 0.5 to 5.2 μm, respectively. (b) Logarithmic base 10 size scale

908

TABLE 2. Chemical compositions of pyroxenes by TEM-EDS analyses

	Nanolite (1μm) A			Nanolite (1μm) B			Nanolite (1μm) C			Ultrananolite[f] (20–30nm)			Glass[g]
Phase	**Opx**	**Aug**	**Sub-calcic aug**	**Opx**	**Aug**	**Sub-calcic aug**	**Opx**	**Aug**	**Aug**	**Ferroaugite**			
Position	**core (x[e])**	**core (y[e])**	**rim (z[e])**	**core**	**core**	**rim**	**core**	**rim**	**rim**				
Elements (atomic%)[a]													
O	58.87	57.61	57.80	58.95	59.83	59.33	60.74	61.27	63.19				64.19
Si	20.01	20.06	19.51	19.51	18.52	19.10	18.78	18.13	17.71				27.39
Ti	0.06	0.18	0.26	0.14	0.30	0.24	0.10	0.27	0.33				0.21
Al	0.54	1.29	1.43	1.22	1.62	1.38	1.02	1.99	2.16				4.44
Fe	5.94	4.83	6.25	6.42	5.30	6.28	5.46	4.85	4.76				0.48
Mn	0.24	0.22	0.25	0.20	0.24	0.25	0.19	0.22	0.19				
Mg	13.54	9.08	9.50	12.67	9.04	10.22	12.53	8.49	7.06				0.13
Ca	0.80	6.74	4.99	0.89	5.14	3.19	1.18	4.79	4.61				0.27
Na													0.91
K													1.98
Total[b]	100	100	100	100	100	100	100	100	100				100
Wo[c]	3.9	32.6	24.1	4.5	26.4	16.2	6.2	26.4	28.1	25	32	27	26.4
En[c]	66.8	44.0	45.8	63.4	46.4	51.9	65.4	46.8	43.0	34	29	29	46.8
Fs[c]	29.3	23.4	30.1	32.1	27.2	31.9	28.5	26.8	29.0	41	39	44	26.8
Oxides (wt%)[d]													
SiO_2	52.99	50.39	48.94	51.38	49.02	49.96	52.11	49.80	50.69				79.61
TiO_2	0.21	0.60	0.87	0.49	1.06	0.83	0.37	0.99	1.26				0.82
Al_2O_3	1.21	2.75	3.04	2.73	3.64	3.06	2.40	4.64	5.25				10.96
FeO	18.81	14.51	18.75	20.22	16.78	19.65	18.12	15.93	16.29				1.71
MnO	0.75	0.65	0.74	0.62	0.75	0.77	0.62	0.71	0.64				
MgO	24.05	15.30	15.98	22.38	16.05	17.93	23.32	15.64	13.55				0.26
CaO	1.98	15.80	11.68	2.19	12.70	7.79	3.06	12.28	12.32				0.76
Na_2O													1.36
K_2O													4.52
Total[b]	100	100	100	100	100	100	100	100	100				100

Notes: (a) The concentration of oxygen was quantified independently. (b) Recalculated to total 100%. (c) Wo = Ca/(Ca+Mg+Fe)atom, En = Mg/(Ca+Mg+Fe)atom, Fs = Fe/(Ca+Mg+Fe)atom. (d) Weight percentages of the oxides were calculated from the atomic percent of cations. (e) The analyzed positions of nanolite are shown in Figure 5f. (f) The solid solution compositions were obtained by subtracting the glass composition from the raw data. (g) The chemical composition of groundmass glass by SEM-EDS spot analyses.

909

910

This is a preprint, the final version is subject to change, of the American Mineralogist (MSA)
Cite as Authors (Year) Title. American Mineralogist, in press.
(DOI will not work until issue is live.) DOI: http://dx.doi.org/10.2138/am-2017-6052CCBYNCND

TABLE 3. Chemical composition of magnetite

	raw	recalculated[b]
Elements (atomic%)		
O	56.84	4.00
Si	0.89	0.06
Ti	2.99	0.21
Al	2.39	0.17
Fe^{2+}	35.66	1.18
Fe^{3+}		1.29
Mn	0.19	0.01
Mg	1.04	0.07
Total	100[a]	7.00
Oxides (wt%)		
SiO_2		0.14
TiO_2		0.61
Al_2O_3		0.31
FeO		44.61
Fe_2O_3		54.20
MnO		0.03
MgO		0.11
Total[a]		100.00
Xusp		0.25

Notes: The analyzed crystals are shown in Figure 7a. (a) Recalculated to total 100%. (b) Recalculated to fit the charge balance.

911

912

TABLE4. Number density of ultrananolite and microlite in Figure 10

		Sub-Plinian pumice			Vulcanian pumice			Vulcanian dense juvenile fragment		
		size range	size interval	n^{*a} (mm^{-3})	size range	size interval	n^{*a} (mm^{-3})	size range	size interval	n^{*a} (mm^{-3})
Pyroxene	**ultrananolite**		-			-		20–30 nm	10 nm	1.7×10^{13}
Fe–Ti oxide	**microlite**	1–5 μm	4 μm	5.7×10^{4}	1–8 μm	7 μm	1.2×10^{7}	1–5 μm	4 μm	1.0×10^{5}
	ultrananolite		-			-		10–20 nm	10 nm	4.1×10^{13}
Fe-rich spot[b]	**ultrananolite**		-			-		1–2 nm	1 nm	$1.9–2.9\times10^{14}$

Notes: Microlite and ultrananolite of Fe–Ti oxide of the Vulcanian dese juvenile fragment were recalculated from the results of Mujin and Nakamura (2014). No plagioclase ultrananolite was observed in any erupted materials. (a) The crystal number densities (n^*) were number of crystals at a size interval per unit area (m^{-3}). (b) The number of Fe-rich spots in the HAADF-STEM image was measured for all through the thin section. The raw number density was thus overcounted compared to that counted on the SEM images of polished surface. We therefore recalculated it by assuming that the section thickness is 100–150 nm.

913

Figure 1 (1 column)

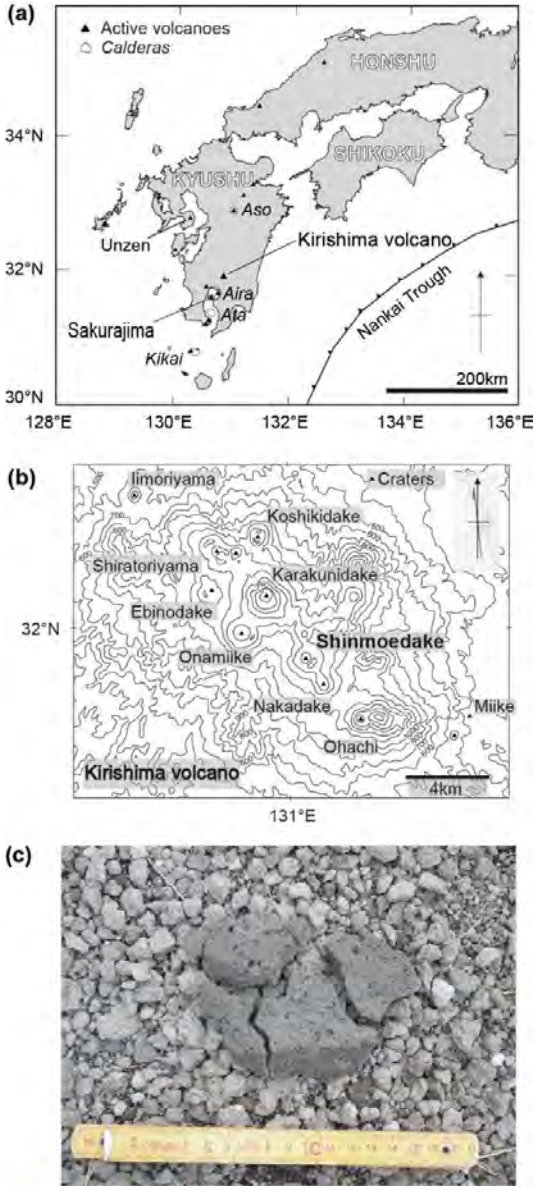

This is a preprint, the final version is subject to change, of the American Mineralogist (MSA)
Cite as Authors (Year) Title. American Mineralogist, in press.
(DOI will not work until issue is live.) DOI: http://dx.doi.org/10.2138/am-2017-6052CCBYNCND

Figure 2 (2 column)

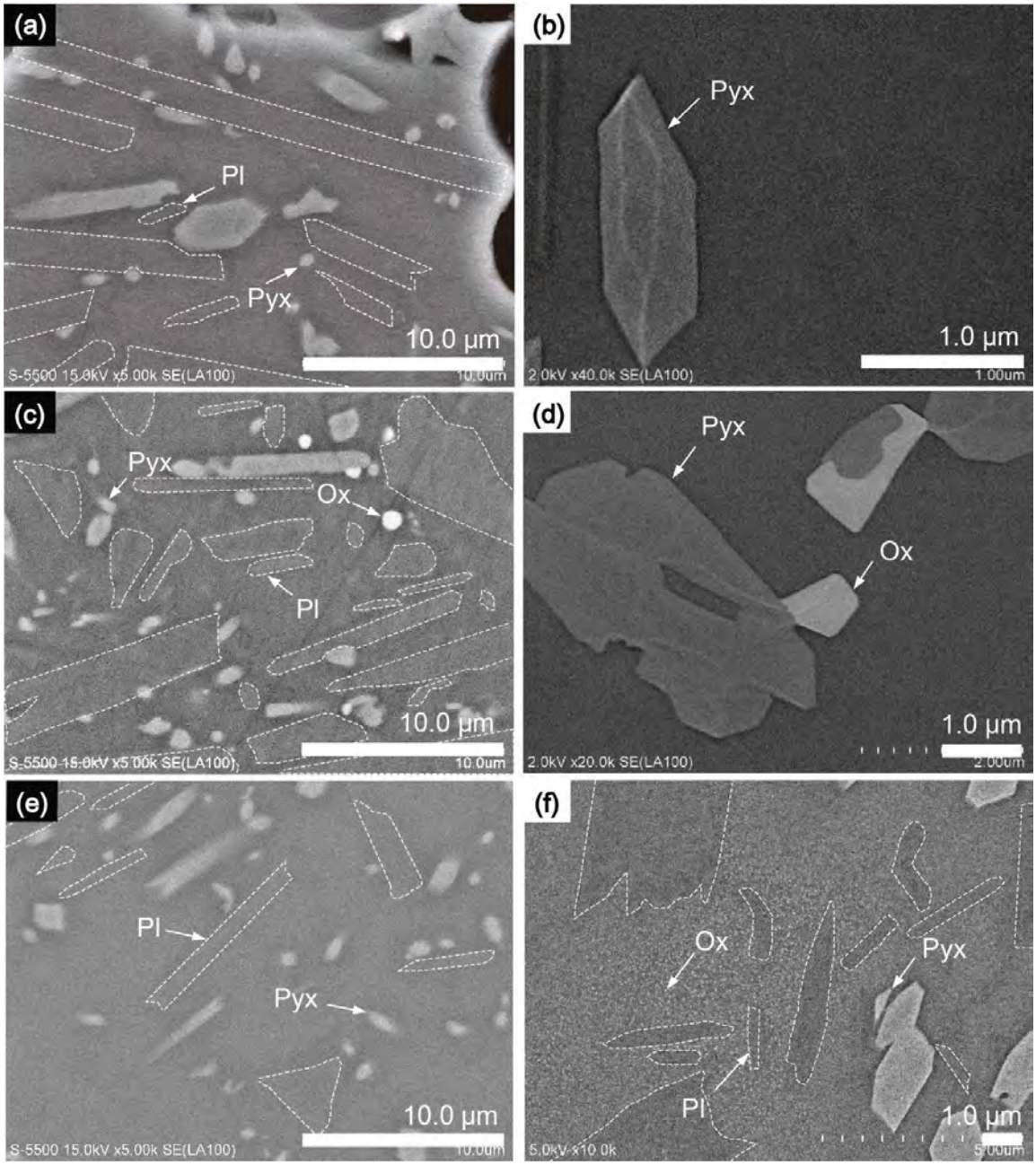

Figure 3 (2 column)

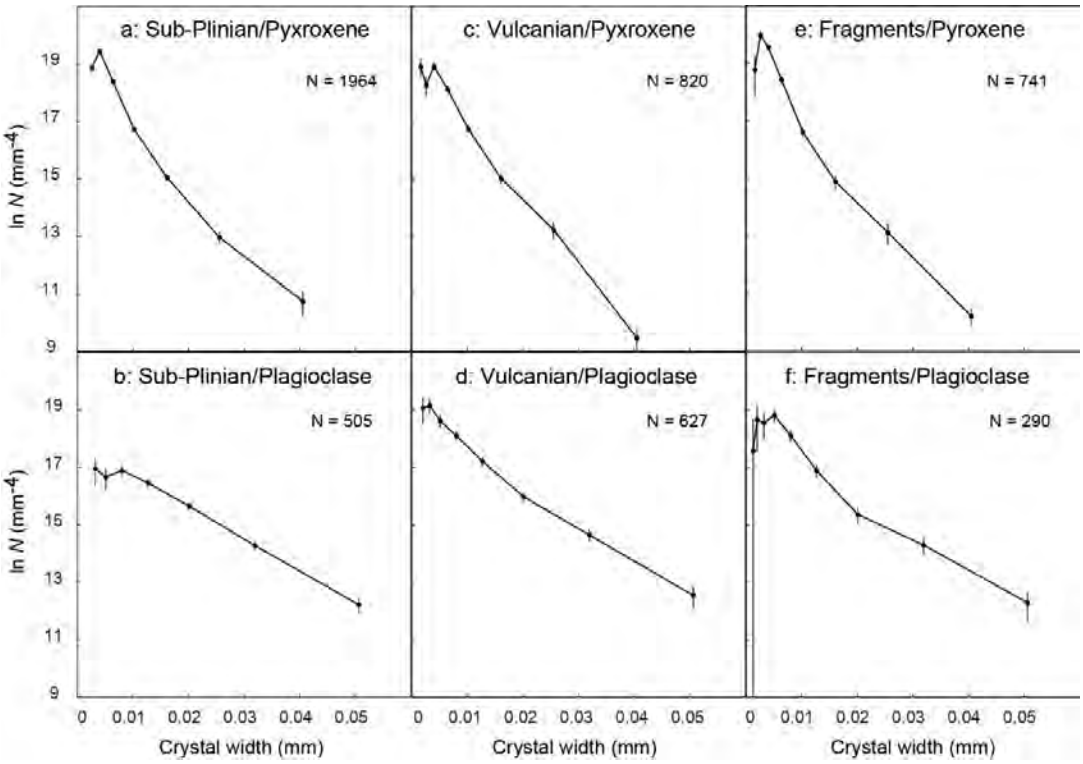

Figure 4 (2 column)

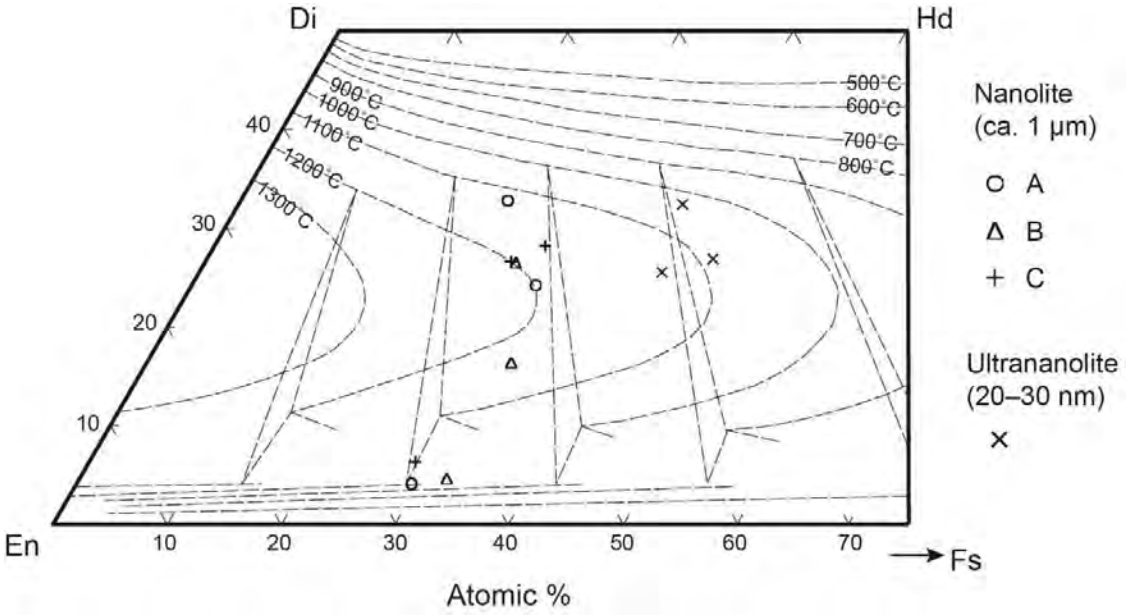

Figure 5 (2 column)

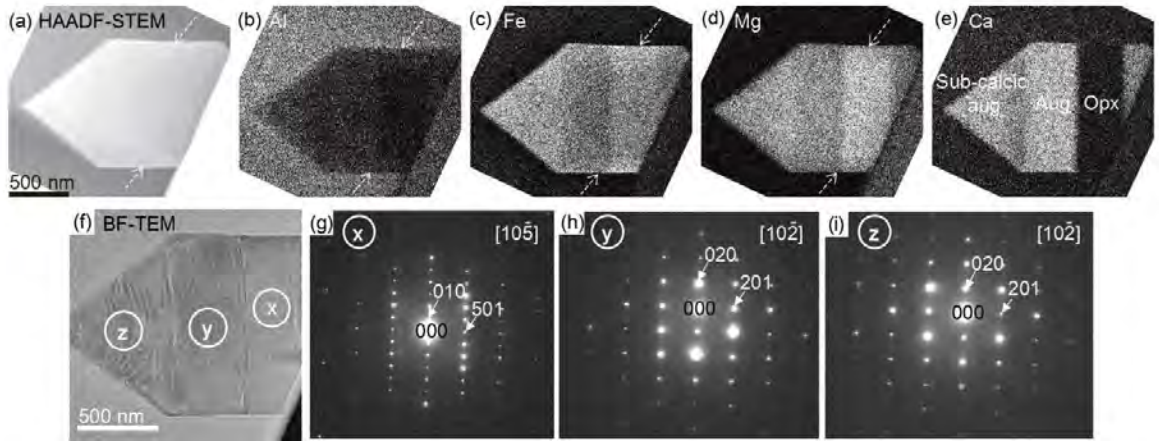

Figure 6 (2 column)

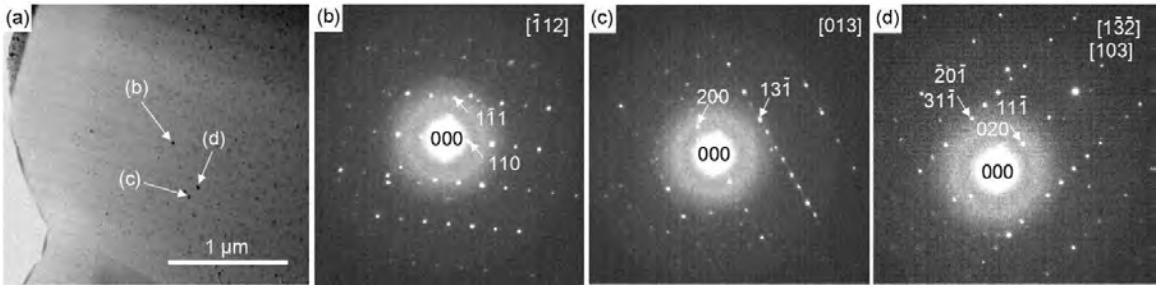

Figure 7 (1 column)

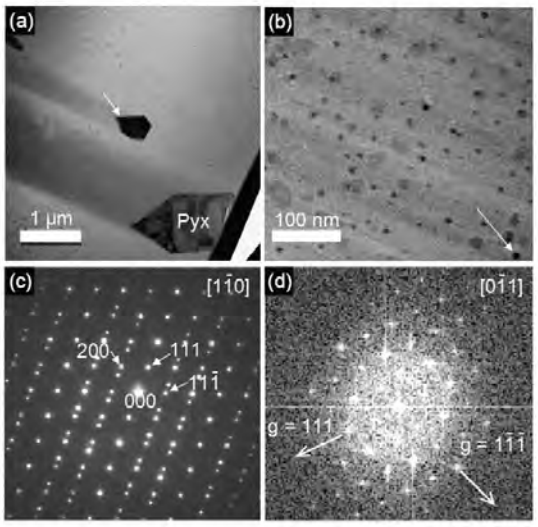

Figure 8 (2 column)

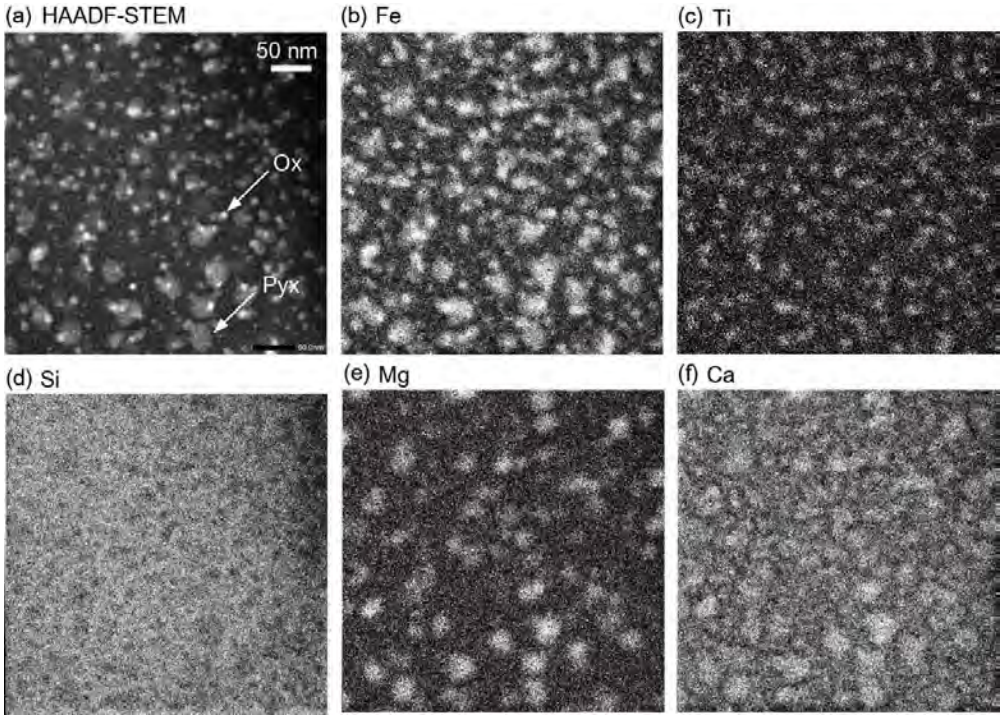

Figure 9 (2 column)

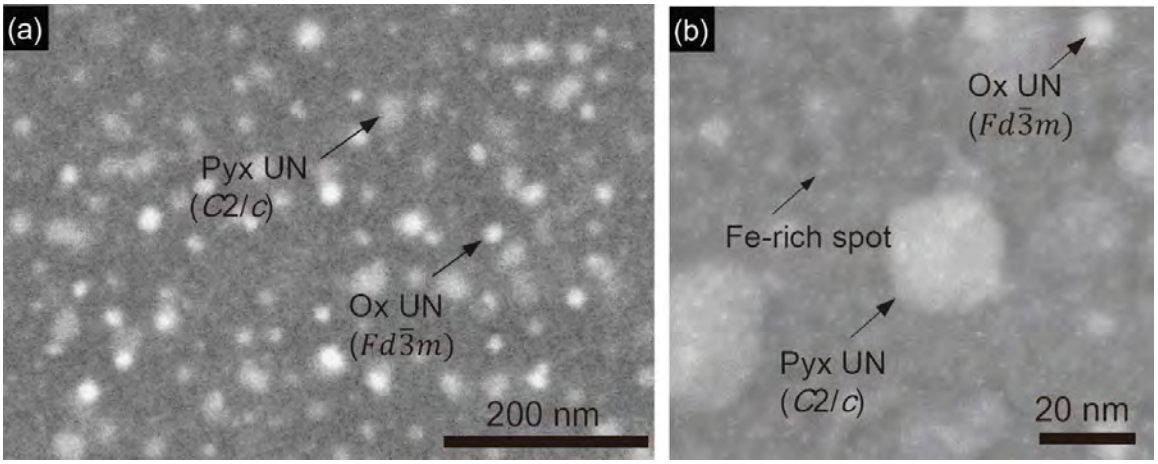

This is a preprint, the final version is subject to change, of the American Mineralogist (MSA)
Cite as Authors (Year) Title. American Mineralogist, in press.
(DOI will not work until issue is live.) DOI: http://dx.doi.org/10.2138/am-2017-6052CCBYNCND

Figure 10 (2 column)

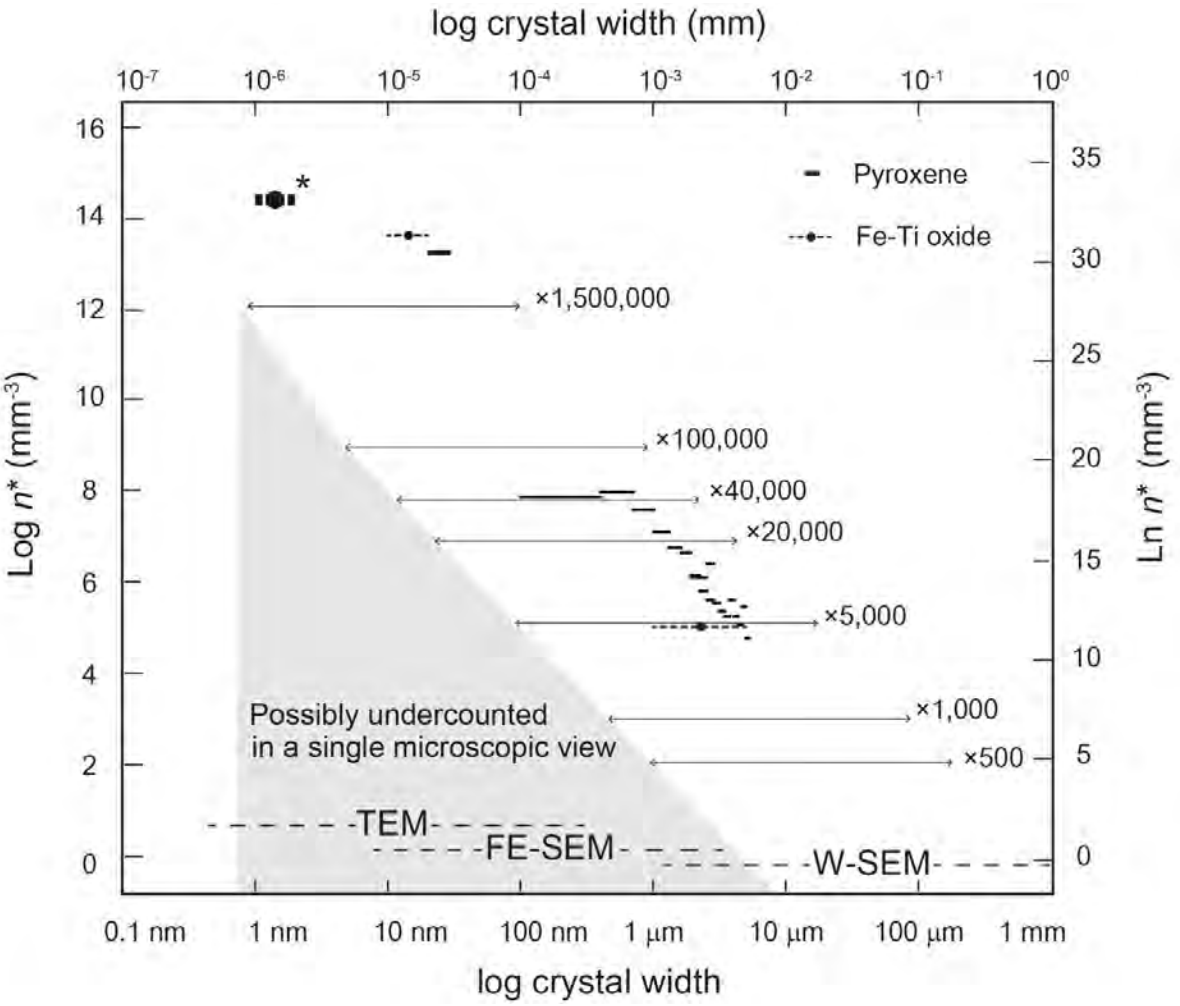

Figure 11 (2 column)

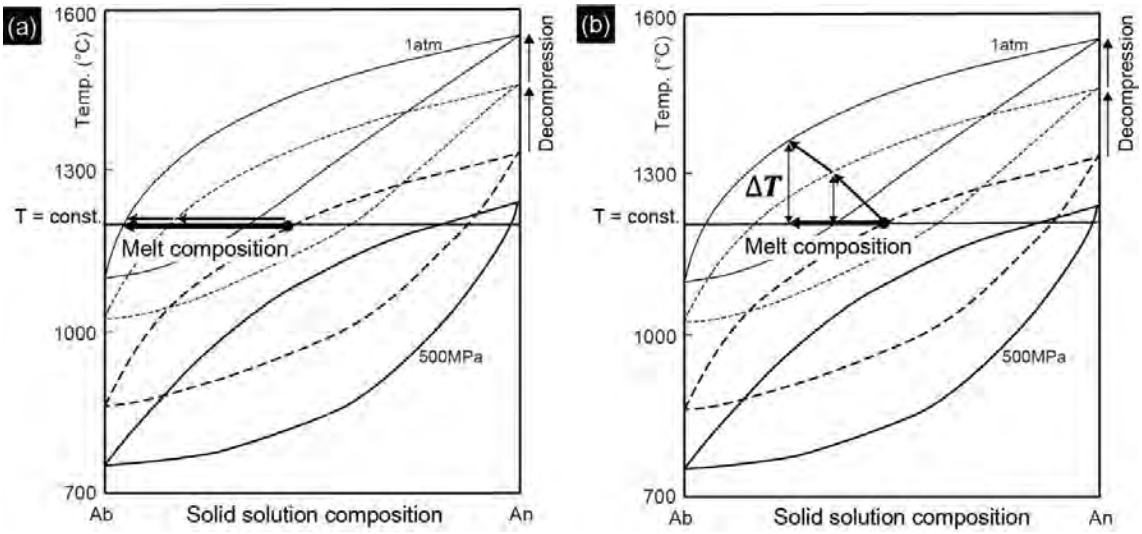

This is a preprint, the final version is subject to change, of the American Mineralogist (MSA)
Cite as Authors (Year) Title. American Mineralogist, in press.
(DOI will not work until issue is live.) DOI: http://dx.doi.org/10.2138/am-2017-6052CCBYNCND

Figure 12 (2 column)

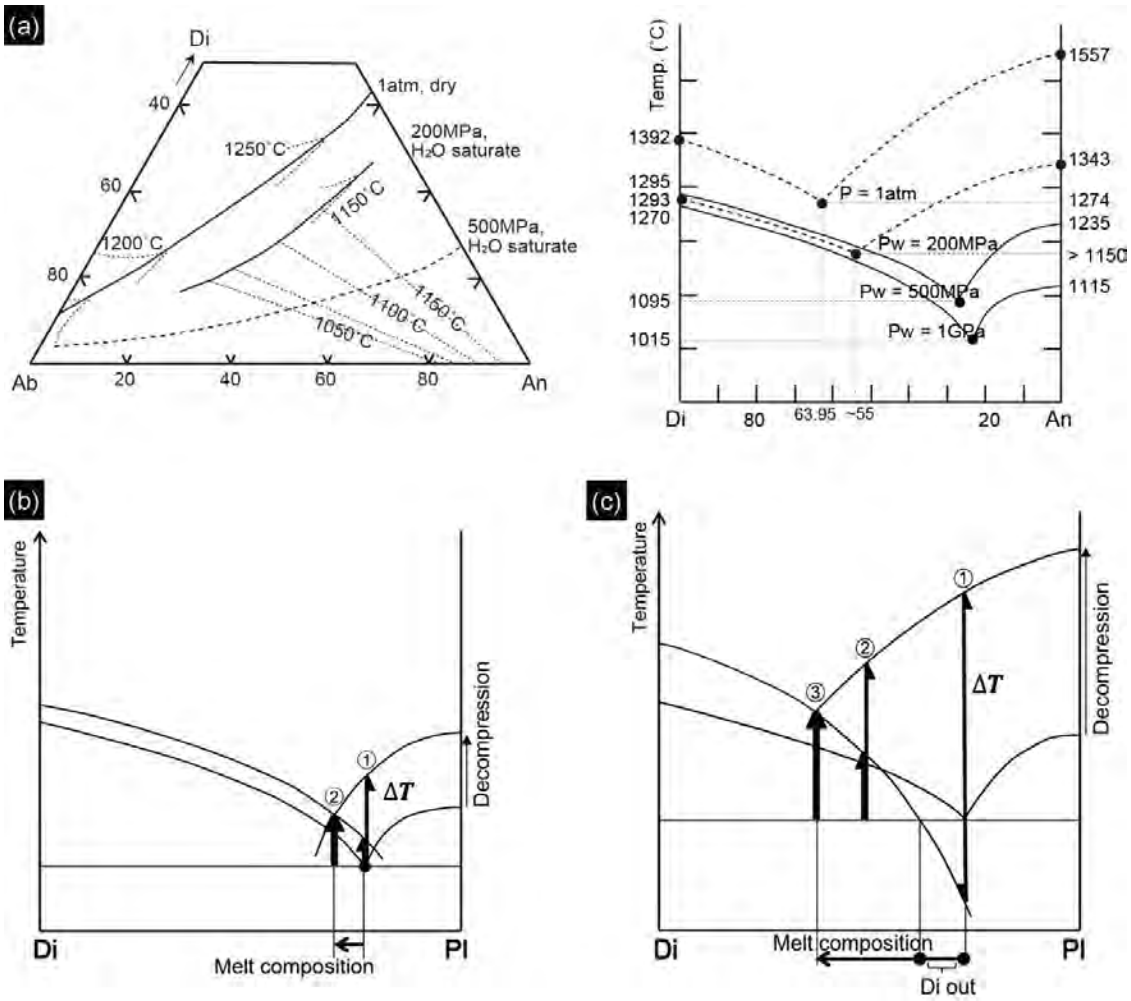

This is a preprint, the final version is subject to change, of the American Mineralogist (MSA)
Cite as Authors (Year) Title. American Mineralogist, in press.
(DOI will not work until issue is live.) DOI: http://dx.doi.org/10.2138/am-2017-6052CCBYNCND

Figure 13 (2 column)